

# Evaluation of morphological indicators of magma supply and segmentation from a seismic reflection study of the East Pacific Rise 15°30'-17°N

Suzanne M. Carbotte, Adina Solomon,<sup>1</sup> and Gustavo Ponce-Correa

Lamont-Doherty Earth Observatory of Columbia University, Palisades, New York

**Abstract.** Hydrosweep bathymetry and multichannel seismic reflection data from two contrasting segments of the East Pacific Rise 15°30'-17°N are used to assess the relationship between crustal structure, morphological indicators of magma supply, and ridge segmentation. From stacked and migrated seismic profiles we evaluate the width and depth of the axial magma lens and the geometry of the seismically inferred extrusive crust, layer 2A. In contrast to other studies, correlation between axial morphology and magma lens characteristics is found with a lens that, on average, is twice as wide and slightly shallower (100-200 m) beneath the unusually shallow and broad southern segment and that shoals and broadens beneath the shallowest part of the northern segment. However, large local-scale variations in lens depth and width are also observed that are not related to morphology. We conclude that magma supply contributes to the regional characteristics of the magma lens beneath a ridge segment, with large variations within a segment due to local processes of magma eruption and delivery. A negative correlation between zero-age extrusive layer thickness and morphology is found with a thinner extrusive layer along the southern segment. In this innermost axial region above the magma lens, factors such as magma pressure, not magma volume in the lens, may govern the thickness of extrusives that accumulate. The width of the zone over which the extrusive layer is built is positively correlated with morphology with a wide zone where extrusives approximately triple in thickness characterizing the southern segment (5-8 km), and a narrower zone (2-5 km) of minor thickening (less than double) along the northern segment and toward ridge segment ends. This relationship could reflect changes in lava flow characteristics in these areas of contrasting magma supply. We find a close correspondence between discontinuities in the narrow axial summit trough and changes in magma lens presence and geometry, indicating a genetic link between the finest-scale tectonic segmentation of the ridge and segmentation of the magma lens. In several locations, discrete magma lenses at different levels within the crust (offset by several hundred meters) are imaged beneath adjacent fourth-order ridge segments.

## 1. Introduction

Systematic variations along mid-ocean ridges in a wide range of geological and geophysical characteristics have led to the hypothesis that the morphology of the ridge crest reflects the local supply of magma to the axis [e.g., *Macdonald et al.*, 1984; *Whitehead et al.*, 1984; *Langmuir et al.*, 1986; *Macdonald and Fox*, 1988; *Scheirer and Macdonald*, 1993]. In this model, enhanced magma supply (both magma production within the mantle and magma volume delivered to and within the crust) is associated with shallow, broad portions of the ridge, with more restricted supply in the deeper regions. Along the fast-spreading East Pacific Rise (EPR) the freshest, least fractured, and most primitive volcanics and most abundant high temperature vents are typically found within the shallow midsections of ridge segments

[e.g., *Francheteau and Ballard*, 1983; *Langmuir et al.*, 1986; *Haymon et al.*, 1991]. Seismic reflection studies show that a horizon marking the magma lens at the top of the axial magma chamber (AMC) is typically detected beneath the shallow, broad regions of the EPR, deepening and disappearing as the ridge deepens and narrows [*Detrick et al.*, 1987, 1993; *Macdonald and Fox*, 1988; *Scheirer and Macdonald*, 1993]. Gravity data show that lower subseafloor densities (indicating thicker crust or hotter mantle) are associated with the shallower regions along the axis [*Scheirer and Macdonald*, 1993; *Wang et al.*, 1996; *Cornier et al.*, 1995; *Hoofft et al.*, 1997]. These observations support the notion that axial morphology can be used as a proxy for magma presence within the crust and underlying mantle.

Seismic reflection data provide information on three crustal parameters which have been discussed as possible direct measures of magma supply: crustal thickness, extrusive layer thickness, and the dimensions of the crustal magma lens. The one location along the EPR where crustal thickness has been mapped in sufficient detail (9°-10°N) indicates thicker crust away from the region of focused magma upwelling inferred from gravity data, possibly owing to strong along-axis transport of melt at crustal levels [*Barth and Mutter*, 1996; *Wang et al.*, 1996]. This

<sup>1</sup> Now at Bryn Mawr College, Bryn Mawr, Pennsylvania.

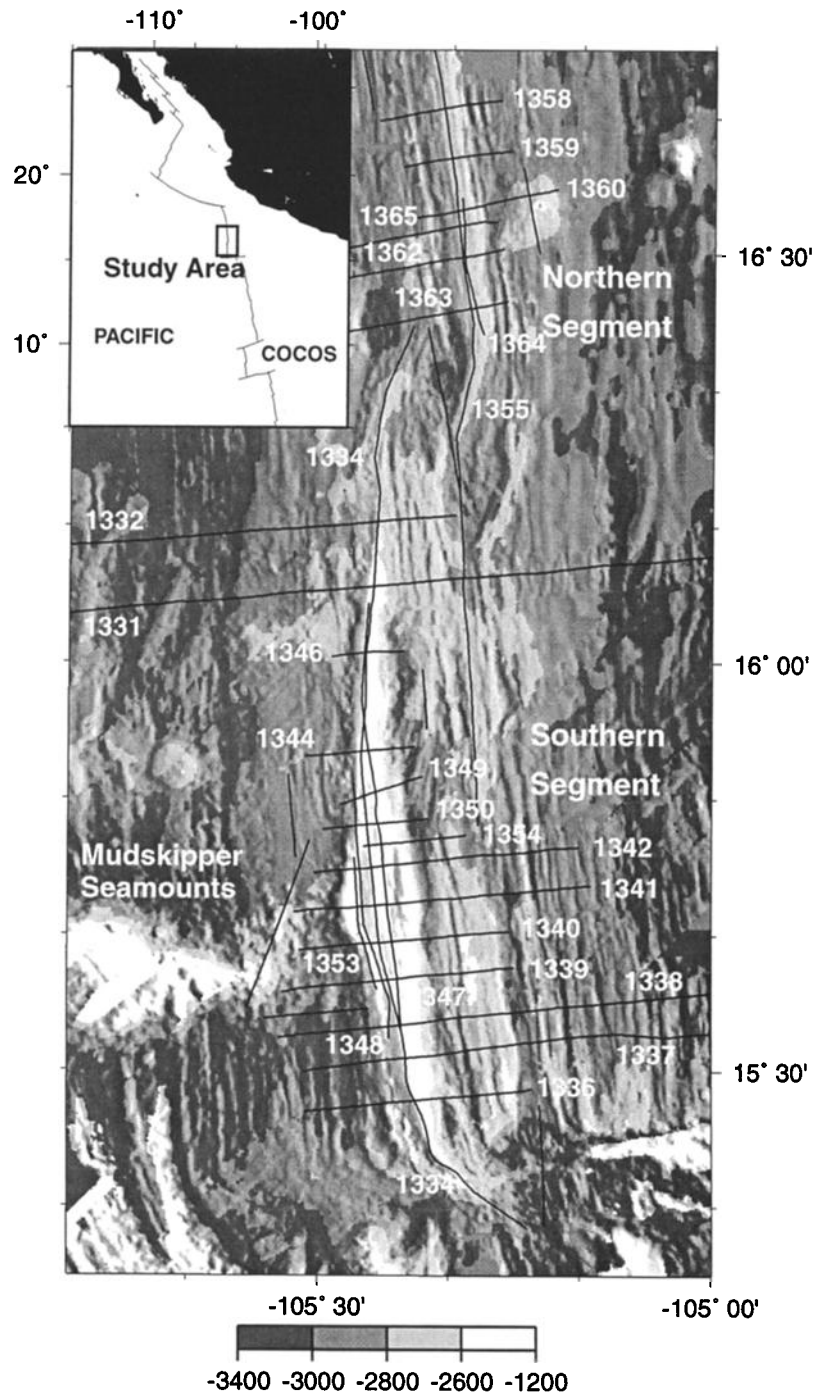


**Figure 1.** Shaded relief bathymetry showing track coverage for seismic reflection survey of the two contrasting ridge segments north of the Orozco fracture zone (labeled southern and northern segment). Line numbers are shown for all lines referred to in text. Illumination is from the southeast. Inset shows location of the study along the northern East Pacific Rise.

study suggests that axial morphology may provide a measure of the supply of magma from the mantle with little direct relationship with crustal thickness. Inferences from extrusive layer thickness have been unclear, and several recent examinations of magma lens properties (depth, width, and inferred melt content) indicate little correlation with axial morphology [Kent *et al.*, 1994; Hooft *et al.*, 1997; Hussenoeder *et al.*, 1996]. However, these previous studies have been located

primarily within regions with modest contrasts in axial morphology, and the relation between morphology and crustal structure has not been fully investigated.

In May 1995 we carried out a bathymetry and multichannel seismic reflection study of the EPR north of the Orozco Fracture Zone. The two segments surveyed (southern and northern segments, Figure 1) display the largest contrast in axial depth and width of any region imaged seismically on the EPR and are ideal

for assessing the relationship between morphological indicators of magma supply and crustal structure. Spreading rates in the region are 85 mm/yr [DeMets *et al.*, 1994], at the fast end of the important intermediate range where an abrupt change in global patterns of axial morphology and gravity is observed [e.g., *Small and Sandwell*, 1992; *Small*, 1994]. The southern segment is an exceptionally shallow and broad portion of the EPR which extends from the Orozco Fracture Zone to a 12-km-offset right-stepping overlapping spreading center (OSC) located at 16°20' N [Sloan, 1991; *Macdonald et al.*, 1992; *Weiland and Macdonald*, 1996]. Enhanced magma supply to this segment is supported by gravity studies which indicate substantially thicker crust (2.25 km) or hotter mantle beneath the central part of the segment [Weiland and Macdonald, 1996]. The Mudskipper seamount chain [Bender *et al.*, 1998; Langmuir *et al.*, 1998], with depths as shallow as 1300 m, extends within 20 km of the axis on the west flank, and the robust morphology of the ridge axis may be associated with tapping of the melt source for this seamount chain. Along the northern segment (north of the 16°20'N OSC) the ridge axis is narrower, deeper, and strongly lineated with prominent faults located along the ridge crest.

Preliminary results from our study are described by Carbotte *et al.* [1998]. In that paper we discuss the influence of spreading rate on crustal structure. Our observations indicate surprisingly little variation in extrusive layer thickness and magma lens characteristics (AMC depth and width) for ridges spreading at a wide range of rates (85-155 mm/yr). This pattern is consistent with the spreading rate invariance of ridges with axial highs noted in studies of ridge morphology and gravity [Small and Sandwell, 1992; Small, 1994; Wang and Cochran, 1995].

In this contribution we analyze the full data set and examine in detail the relationship between crustal structure, morphological indicators of magma supply, and ridge segmentation. First we describe the detailed morphology and tectonic setting of the two ridge segments. Rapid and abrupt changes in ridge geometry have occurred along the southern segment within the past 100 kyr, including a ~7-10-km ridge jump and propagation north of a small offset, which we associate with increased proximity of the Mudskipper seamount melt source. Along the northern segment, axial morphology evolves into that characteristic of intermediate-spreading ridges with elevated fault blocks bounding the edges of the axial high. Seismic data from both segments are used to map the depth and width of the magma lens and the thickness of layer 2A, the seismically inferred extrusive crust. We conclude that the large-scale morphology of a ridge segment does provide some indication of magma lens characteristics but that within a segment, large local-scale variations in lens depth and width are found which likely reflect processes of magma delivery to and removal from the lens. We find a negative correlation between the thickness of the extrusives at zero age and axial morphology. A positive correlation between morphology and the width of the extrusive layer accumulation zone is found, with an accumulation zone that narrows toward the ridge segment ends and along the deeper northern ridge segment. Our dense seismic coverage reveals a strongly three-dimensional magma lens beneath the ridge axis and a close correspondence between segmentation of the magma lens and small offsets of the axial summit trough. We find evidence for discrete lenses associated with adjacent ridge segments bounded by small offsets of the axial summit trough and for multiple lenses at different levels within the crust. Finally, the distribution of the magma lens at the southern segment suggests connection between magma plumbing for the current ridge axis and the Mudskipper seamount chain.

## 2. Bathymetric Data

Hydrosweep bathymetry collected simultaneously with the multichannel data are merged with existing SeaMARC II and SeaBeam bathymetry data [Macdonald *et al.*, 1992] to produce detailed maps of the two ridge segments and adjoining ridge flank terrain (Plate 1). SeaMARC II side-scan sonar data (courtesy of K. C. Macdonald) are used to identify the axial summit trough (AST) along these ridge segments (Plate 1 and Figure 2). This narrow depression typically corresponds with the region of most recent volcanism and hydrothermal activity [Macdonald and Fox, 1988; Haymon *et al.*, 1991]. It is interpreted to result from volcanic collapse processes associated with seafloor eruptions rather than the tectonic stretching associated with the ridge flank terrain [Haymon *et al.*, 1991; Fornari *et al.*, 1998]. Devals (deviations in axial linearity) [Langmuir *et al.*, 1986] or discontinuities in this summit trough define the finest-scale tectonic segmentation of the ridge axis [Macdonald *et al.*, 1988; Haymon *et al.*, 1991]. In sections 2.1-2.2 we describe the detailed morphological features of the region which provide the tectonic setting for our seismic data.

### 2.1. Southern Segment

The southern segment shoals rapidly from the western Orozco-EPR ridge transform intersection to a broad, flat axial plateau, 3-4 to 10 km wide, which lies at a markedly uniform elevation of 2320 ± 10 m (Figure 1 and Plate 1). At its widest point, from 15°40' to 15°44'N, a split seamount is found on the edges of the axial plateau, rising 100-200 m above the innermost region. Low densities beneath the ridge axis inferred from gravity data are focused beneath this broadest part of the ridge [Weiland and Macdonald, 1996]. A second, smaller volcanic edifice up to 70 m high is found centered within the axial plateau farther to the north at 15°50'N. Volcanic constructional edifices of these scales are unusual for the axial high of the fast-spreading EPR, where efficient along-axis plumbing may typically prevent local centers of volcanism from developing.

The axial summit trough roughly follows the center of the axial plateau with considerable variation in width and complexity (Plate 1). From steps or changes in the width of the AST we identify devals at 15°38', 15°45', 15°48', 15°53'-55', and 15°59'N. The 15°38'N deval corresponds with a widening of the AST to the west. At 15°45'N the AST steps east just north of the broad split seamount portion of the ridge. Farther north, the trough steps east again and bisects the 70-m-high axial volcanic mound. The 15°53'-55'N deval is composed of three en echelon overlapping segments of the summit trough. The largest discontinuity along the southern ridge segment is a right-stepping offset of 1 km found at 15°59' - 16°00'N (Figure 2). This deval has a subtle bathymetric signature, with the ridge narrowing and deepening slightly at the offset, becoming broader and shallower for ~5 km directly to the north.

Centered ~10 km east of the axial high, a broad ridge, distinct from surrounding abyssal hills, with similar width (up to 8 km) and flat-topped morphology to the current axial plateau, is found (Figure 1 and Plate 1). This off-axis plateau extends parallel to the current axis from the Orozco Fracture Zone to ~15°47'N. Directly north of this plateau, a series of three curving basin and ridge pairs are found which form a swath of ridge-oblique terrain aligned 10-15° to the trend of AST (350°). The morphology of these features is characteristic of the relict ridge tips and overlap basins left on the ridge flanks with propagation of an overlapping spreading center [Macdonald *et al.*, 1988; Lonsdale, 1989;

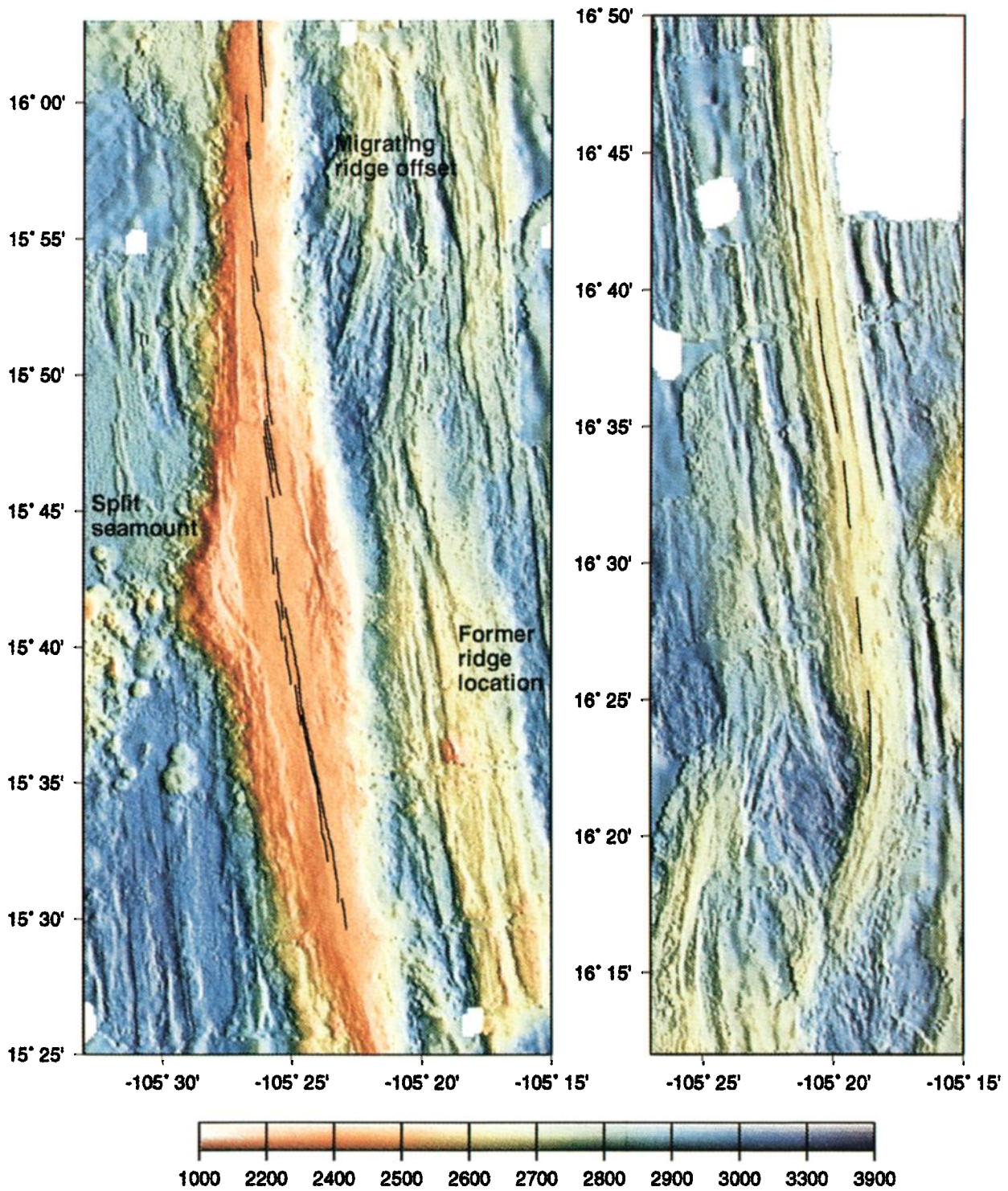


**Plate 1.** Detailed bathymetry of the axial region for the (left) southern and (right) northern ridge segments. Hydrosweep bathymetry data collected simultaneously with the multichannel seismic data are merged with the preexisting bathymetric compilation for the region [Macdonald *et al.*, 1992]. Data are gridded at a 100 m interval using the gridding algorithm of Smith and Wessel [1990] and displayed as shaded relief with illumination from the southeast. The axial summit trough identified from SeaMARC II side-scan sonar data (courtesy of K. C. Macdonald) is shown in thin black line. With the large contrast in axial morphology of these two segments the region is ideal for evaluating the relation between morphological indicators of magma supply, upper crustal structure and the characteristics of the axial magma lens.

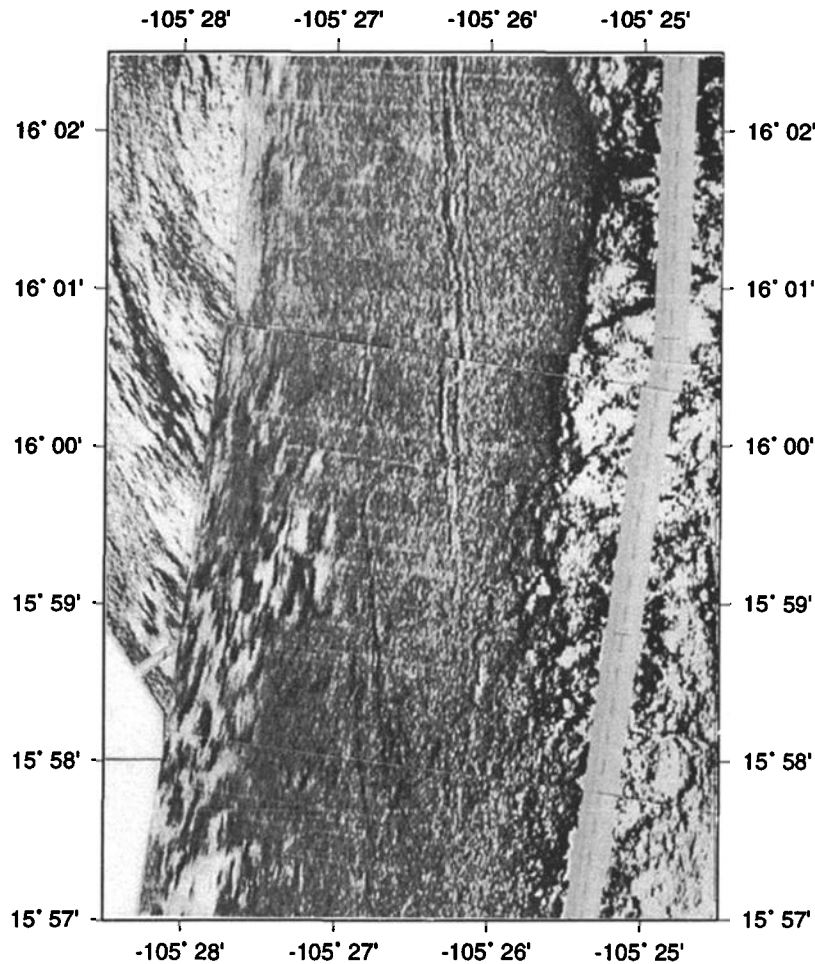


**Figure 2.** SeaMarc II side-scan sonar data for the 15°59'N deviation in axial linearity (deval) showing a 1-km offset of the narrow axial summit trough. Areas of high reflectivity are in dark tones. Data courtesy of K. C. Macdonald.

*Carbotte and Macdonald, 1992*] and indicates the presence of a migrating nontransform discontinuity initially located at 15°47'N.

## 2.2. Northern Segment

Along the northern segment the EPR progressively shallows from the 16°20'N OSC to a local minimum depth of 2645 m at 16°29'-31'N. North of this shallowest point, the ridge crest becomes strongly lineated, and a rifted axial morphology develops. A pair of fault scarps extend along the edges of the ridge crest and bound fault blocks elevated 15-25 m above the innermost axial zone. A central ridge is located between the elevated rift shoulders that in places is transected by a linear scarp. We tentatively identify this lineation as an AST although it is difficult to positively identify this feature as a depression rather than a single fault from the side-scan data. With the equivocal nature of this lineation we do not attempt to define fine-scale tectonic segmentation along this segment.

The cross-axis shape of the ridge north of 16°31'N is similar to that of the rifted axial high segments of the intermediate-spreading Southeast Indian Ridge at ~100°E and the Galapagos Spreading Center at 86°W [*Sempere et al., 1997; Klitgord and Mudie, 1974*]. On the basis of morphology it appears that the transition from fast to intermediate spreading regimes for the EPR occurs in this region.

## 2.3. Recent Tectonic History

The complete multibeam coverage of the axial region obtained during our cruise provides new information on the recent tectonic history of the southern segment with important implications for interpretation of crustal structure within the region. On the basis of ~20% asymmetry in the width of the Brunhes anomaly with respect to the current axis, *Weiland and Macdonald [1996]* conclude that a westward ridge jump occurred along the southern segment in the past 0.3-0.15 Myr. From the morphological similarity to the current axis we infer that the east flank plateau was the former ridge axis location. The locus of spreading jumped west 7-10 km to its present location presumably in response to increased proximity of the melt source associated with the Mudskipper seamount chain as the EPR migrated northwest in the mantle reference frame [*Gripp and Gordan, 1990*]. Bathymetry show a crosscutting relationship between the current axial high and adjacent abyssal hills on the west flank with the axis trending 5° oblique to and overprinting more northerly trending abyssal hills (Plate 1). This crosscutting relationship indicates that spreading has been established at the current location for, at maximum, 85 to 105 kyr (time corresponds with width of axial plateau to first obliquely oriented abyssal hill).

The nontransform offset located at ~15°47'N may have existed

prior to or may have developed as a result of westward jump of the ridge axis south of this location. Following the ridge jump, this offset rapidly migrated north at a rate of  $\sim 240$  mm/yr (estimated from the average trend and width of the relict basin-ridge terrain). The 15°59'N deval is located just north of the northernmost relict basin-ridge pair and may be the current site of this migrating offset. The tectonic history described above implies that accretion along the southern segment has been focused beneath the current axial plateau for  $\sim 100$  kyr and that the crustal structure of the axial region may not be typical of the earlier phases of spreading in this location.

### 3. Seismic Experiment and Data Analysis

Multichannel seismic (MCS) reflection data were obtained using a tuned, 10-gun 3005-cu.in. array and a 4-km-long, 160-channel digital streamer with a 25-m group spacing. Data lengths of 10 and 8 s were recorded with a 2 ms sampling interval in SEG-D format. A 20-s shot interval provided 50-m shot spacing for the average ship speed of 5 knots. With merging of navigation data, shot gathers were sorted into 12.5-m bins generating approximately forty-fold common midpoint (CMP) gathers.

Six along-axis lines were shot, providing coverage from just south of the western Orozco-EPR ridge transform intersection to 16°55'N (Figure 1). Along-axis lines 1334 and 1355 on the southern and northern segments, respectively, were shot following as closely as possible the center of the axial high and the axial summit trough where it could be detected. Additional along-axis lines were run spaced 0.5-1.5 km within the broader portions of the axial high along both ridge segments. Twenty cross-axis lines 10 to  $>30$  km long were shot located at  $\sim 5$ -10 km intervals along both ridge segments. During our survey, brute stacks obtained in real time were used to determine optimal locations for the across-axis lines.

The MCS data image a bright reflection from the top of the axial magma chamber, as well as a refracted arrival from the base of layer 2A. The layer 2A event arises from a steep velocity gradient in the shallow crust within which *P* wave velocities rapidly increase from  $\sim 2.4$  to 5 km/s [e.g., Vera *et al.*, 1990; Christeson *et al.*, 1994]. The layer 2A-2B boundary has been variously interpreted as the lithologic boundary between low-density extrusive rocks and higher-density dikes [Toomey *et al.*, 1990; Christeson *et al.*, 1992, 1994; Harding *et al.*, 1993; Vera

and Diebold, 1994] or as a porosity horizon within the extrusive layer associated with a fracture front or hydrothermal alteration [e.g., McClain *et al.*, 1985; Wilcock *et al.*, 1992]. The bulk of the available evidence, albeit sparse and indirect, supports the lithologic model, and in most recent seismic studies, layer 2A is used as a proxy for the extrusive crust [e.g., Carbotte *et al.*, 1997; Hooft *et al.*, 1997].

In addition to the AMC and layer 2A arrivals a Moho reflection was observed intermittently in our data, predominantly on the short, ridge-parallel segments run between cross-axis lines. The major exception was line 1331 where excellent Moho was imaged from the edge of the axial high for over 20 km on the ridge flanks. However, given the rare occurrence of Moho in most of our data, we did not attempt to map this feature and have restricted this study to the AMC and layer 2A arrivals.

To image these events, stacking velocities were obtained using detailed velocity analysis of selected CMP gathers (every 10 to 50). For each gather inspected, constant velocity normal move-out was applied at a range of velocities, and the velocities which best flattened the layer 2A event in the vicinity of its terminating caustic and the AMC event were identified. From this analysis a stacking velocity function which varied with two-way travel time for the seafloor, layer 2A event, and AMC was constructed. Semblance methods are inadequate for velocity analysis for these data because of interference effects of seafloor scattering and the nonhyperbolic nature of the 2A arrival. During stacking, an outside mute was applied beyond offsets of 3000 m to minimize the effects of extreme stretching of the 2A event at the farthest offsets. Stacked sections were migrated using a frequency-space (FX) migration algorithm. FX migration is well suited to handle large lateral velocity contrasts such as those associated with the changing structure of layer 2A at the ridge axis. For migration we used a velocity model derived from the on-axis velocity-depth profile of Vera *et al.* [1990] modified for the location of the base of layer 2A along each line.

With this procedure, good images of the base of layer 2A and the AMC were obtained for along-axis lines 1334 and 1355. However, for cross-axis lines and additional along-axis lines, optimal images were obtained by merging migrated constant velocity stacks for the layer 2A event with FX-migrated sections for the AMC using the approach described in detail by Vera and Diebold [1994]. First, panels of constant velocity stacked sections

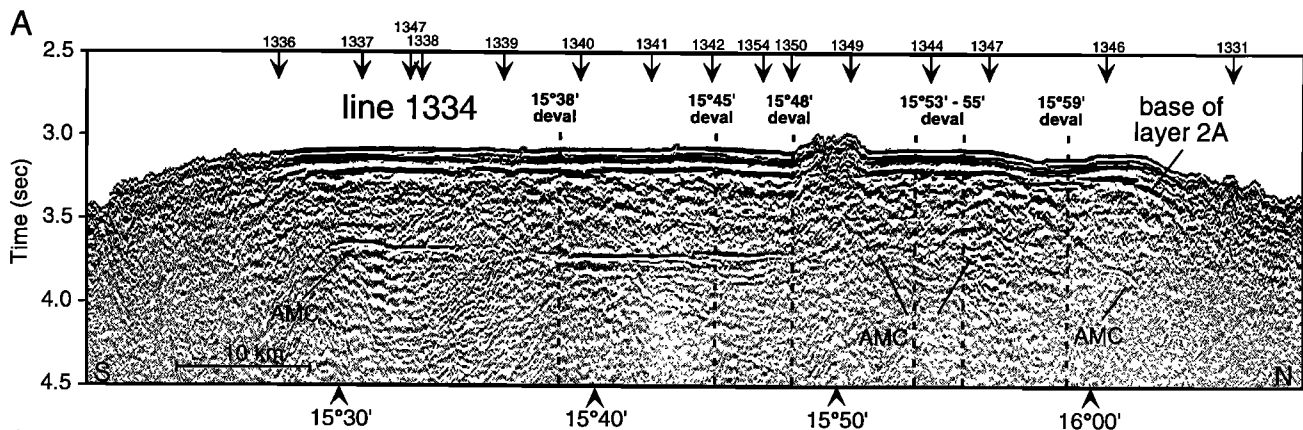


**Figure 3.** (a-d) Representative seismic images showing the AMC reflector and the base of seismic layer 2A along the axis of the southern and northern segments. Locations of seismic profiles are shown in Figure 1. Note that only portions of these profiles are reproduced. Because of difficulties displaying long axial lines, we stack every four common midpoint (CMP) gathers for along-axis lines 1334 and 1355 and every two CMPs for line 1347.

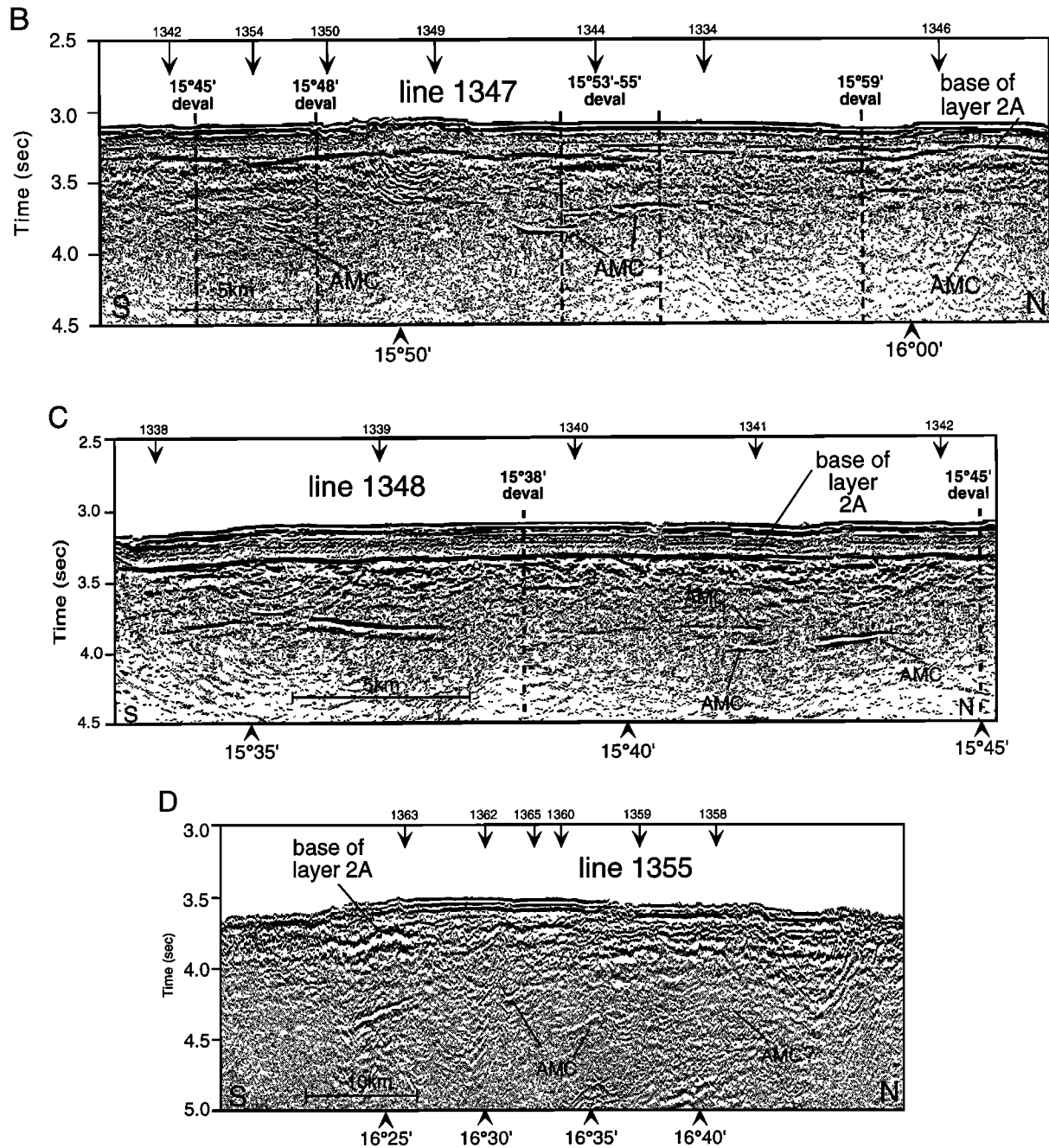


Figure 3. (continued)

were created for each line for velocities ranging from 1520 to 1750 m/s at 15 to 25 m/s increments. From these panels the constant velocity stacks which best focused the layer 2A event at different locations along the profile were chosen, and a single constant velocity stack section was created and migrated. A time window encompassing the layer 2A event was extracted from this section and merged with the migrated section for the seafloor and AMC event. Processing was carried out using a combination of in-house code for velocity analysis and stacking and the OMEGA software package for migration.

In Figures 3-5, examples of final migrated stacks are presented. For each line the AMC and layer 2A events are digitized and converted to depth with a simple velocity model constructed from expanding spread profile (ESP) data for the

ridge axis and flanks at 9°N [Vera *et al.*, 1990]. For the on-axis region, interval velocities used for depth conversion are given in Table 1 and compared with velocities obtained from sonobuoys collected along axis during MCS acquisition. Interval velocities are calculated from velocity-depth models shown in Figure 6 following the approach of Slotnick [1959] for constant velocity gradients.

Uncertainties in layer 2A and AMC depth estimates arise from a number of sources and include errors associated with determining the correct travel times to these events (stacking and picking errors) and with uncertainties in crustal velocities for depth conversion. Stacking errors may be quite large for the layer 2A event and, in the absence of velocity-depth information for individual CMP gathers, are very difficult to quantify. Detailed

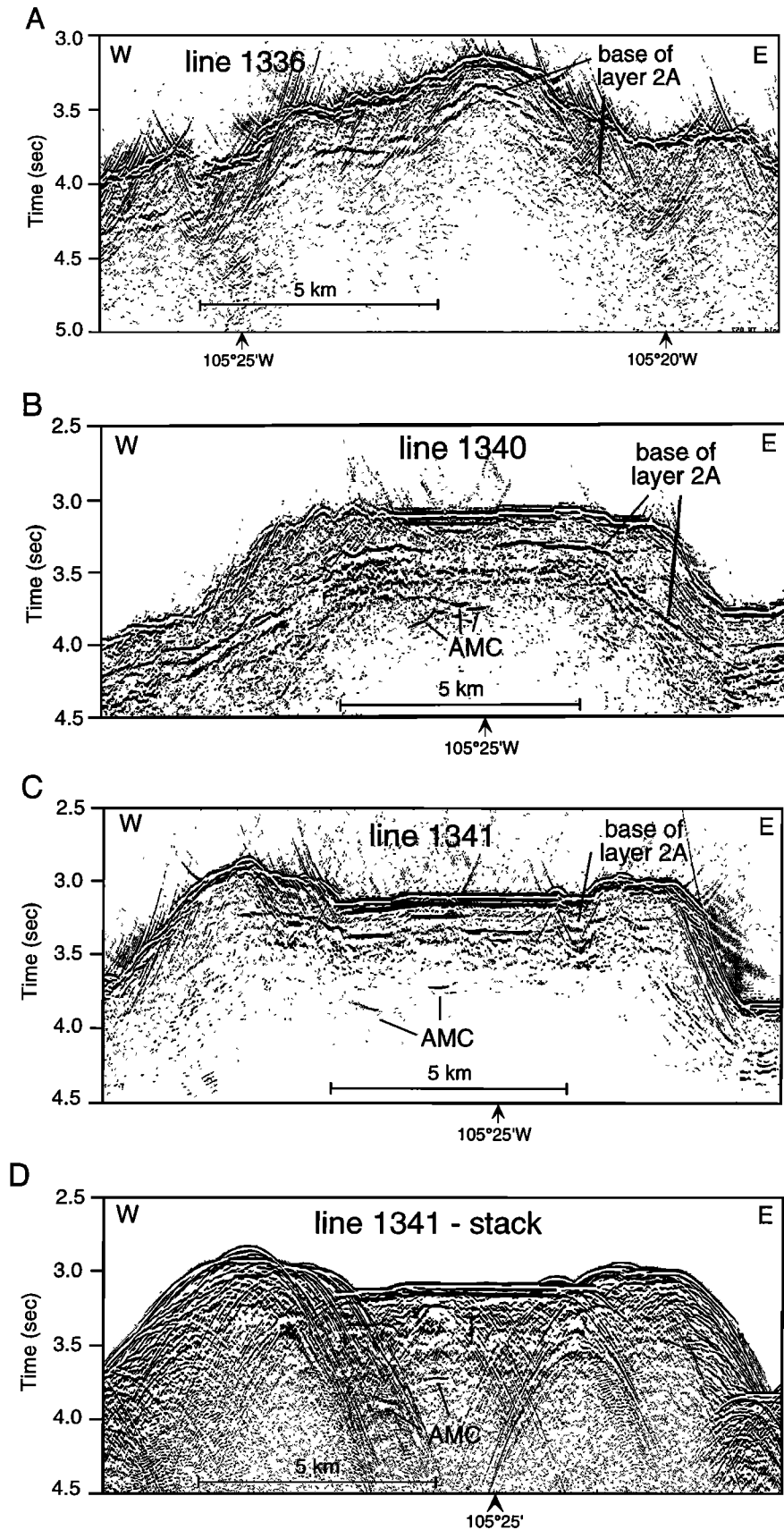


**Figure 4.** Representative cross-axis images of the (a-e) southern and (f-h) northern segments. Locations of seismic profiles are shown in Figure 1. Note that only portions of these profiles are reproduced. An unmigrated section for line 1341 is included to show the two distinct diffractive AMC events at this location. We include an unmigrated section for line 1362 (Figure 4g) showing the characteristic broad diffractive AMC event which, with migration, is focused into a narrow region along the northern segment.

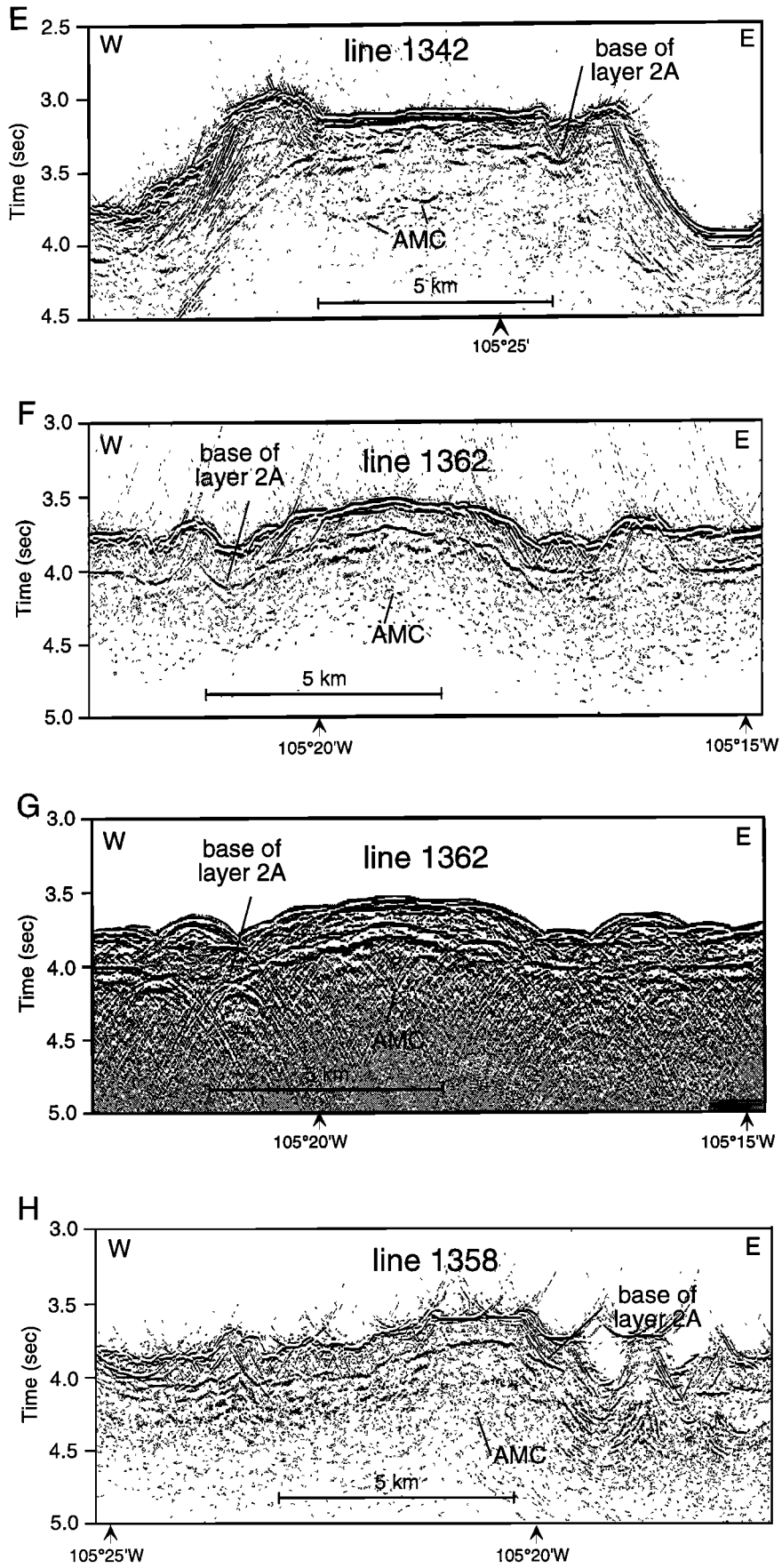


Figure 4. (continued)

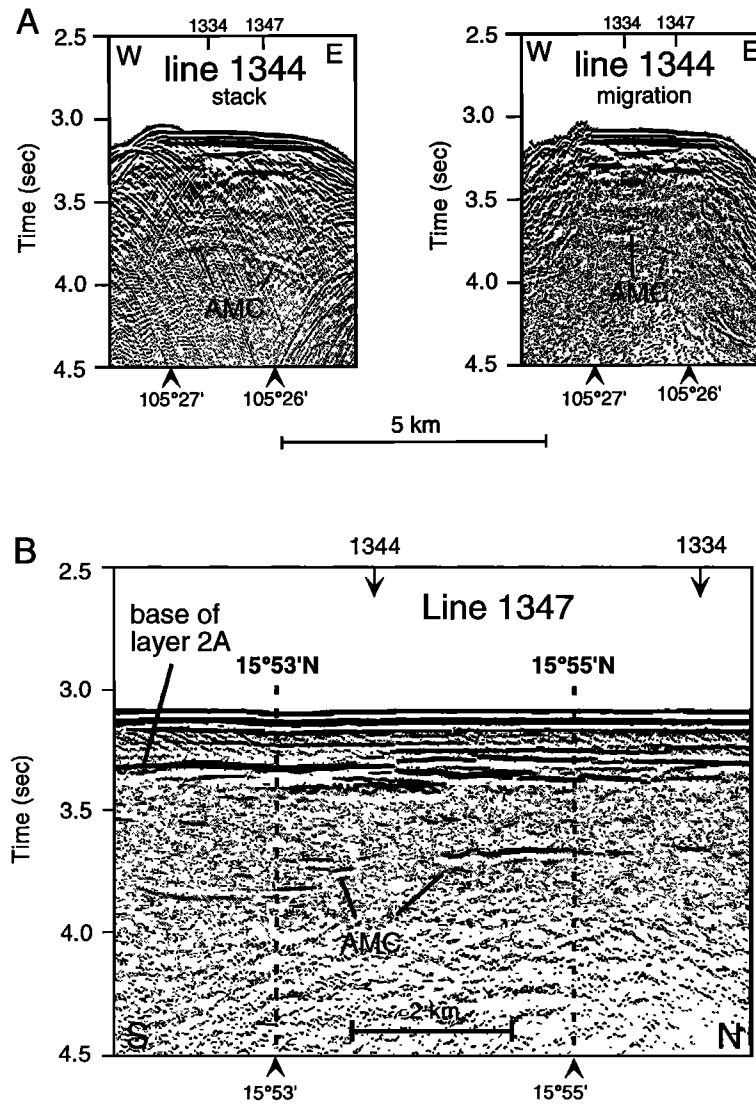


Figure 5. (a) Cross-axis line 1344 and (b) intersecting along-axis line 1347 indicate that multiple lenses at different levels in the crust are present in the vicinity of the 15°53'-55'N deval.

Table 1. Interval Velocities

	Location <sup>a</sup>	Average Interval Velocity for Layer 2A <sup>b</sup>	Average Interval Velocity for Layer 2B <sup>b</sup>
ESP 5 <sup>c</sup>	9°36'N	2.563	5.42
		3.175	5.506
SB107	15°47'N	2.62	5.71
SB110	15°30'N	2.76	5.503
SB119	15°37'N	2.92	5.49
SB129	16°40'N	2.89	5.57
This study		2.75	5.506

<sup>a</sup>Location corresponds with approximate midpoints of sonobuoy and expanding spread profiles.

<sup>b</sup>Average interval velocities are calculated from velocity-depth functions shown in Figure 6 following treatment of Slotnick [1959] for constant velocity gradient layers.

<sup>c</sup>From Vera *et al.* [1990]. This velocity model includes a step in the gradient zone defining the base of layer 2A. Two average velocities given here are for layer 2A defined to the top of the step and base of the step.

refraction studies for upper crustal structure at 9°N [Christeson *et al.*, 1994] show considerable spatial variation in the thickness and structure of the gradient zone defining the base of layer 2A. If this variability characterizes our area as well, we expect that the part of the layer 2A gradient zone imaged may change along our profiles [e.g., Christeson *et al.*, 1996]. A recent study of upper crustal velocity structure from 17°S (Hussenoeder *et al.*, Fine-scale seismic structure of young upper crust at 17°20'S on the fast-spreading East Pacific Rise, submitted to *Journal of Geophysical Research*, 1999) suggests that the differences in layer 2A thickness obtained by Hooft *et al.* [1996] and Carbotte *et al.* [1997] for the same area reflect stacking of different portions of the gradient zone defining the base of layer 2A. Inspection of the range of constant velocity stacks for which the layer 2A event is well focused in our study area suggests typical stacking errors of the order of  $\pm 0.01$  s two-way travel time (TWTT) for the axial region, although much larger uncertainties likely characterize off-axis regions where significant topographic effects are expected. For more detailed discussion of uncertainties

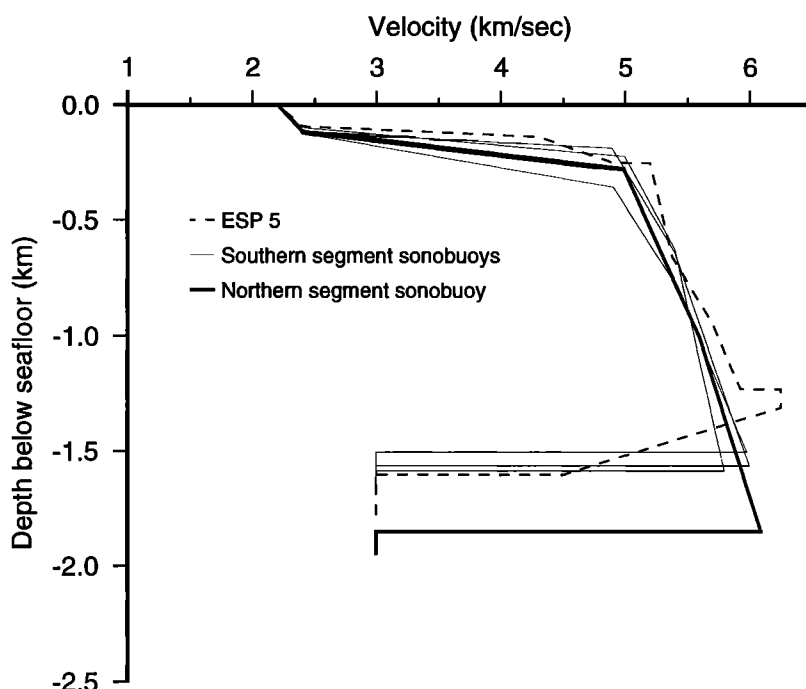


**Figure 6.** Comparison of velocity-depth models obtained from sonobuoy data collected during seismic acquisition with the expanding spread profile (ESP) 5 model of *Vera et al.* [1990] for the EPR at  $\sim 9^{\circ}30'N$ . Interval velocities used for depth conversion are derived from these models (Table 1).

associated with stacking layer 2A we refer the reader to *Harding et al.* [1993] and *Carbotte et al.* [1997].

From repeat picks of the AMC and layer 2A we estimate picking errors of  $\pm 0.012$  s two-way travel time for both events. Considering stacking and picking errors and a range of possible upper crustal velocities from 2.55 to 2.95 km/s (Table 1), we assign an error of  $\pm 30$  m for layer 2A thickness measurements. From a range of layer 2B velocities from 5.45 to 5.65 km/s we assign an error of  $\pm 50$  m for the AMC event.

AMC depths obtained for all lines are shown overlaid on the bathymetry in Plate 2. Depths to the AMC reflector agree well at the intersections between across- and along-axis lines (with the exception of mismatches of  $>100$  m on lines 1342 and 1365, which likely reflects three-dimensional effects associated with crossing the edge of the magma lens). Line drawing interpretations for along-axis lines 1334 and 1355 are presented in Figure 7 and for axis-crossing lines in Figure 8. AMC characteristics for each cross-axis line are given in Table 2. In Tables 3 and 4, characteristics of layer 2A for both ridge segments are compared. In Table 5, AMC and layer 2A parameters are compared with other regions of the EPR.

In section 4 we describe our observations regarding the distribution, the depth and width of the magma lens, the thickness of layer 2A, and the pattern of accumulation of this layer at both ridge segments.

## 4. Observations: AMC Event

### 4.1. Southern Segment

An AMC reflector is observed beneath much of the southern ridge segment from  $15^{\circ}29'N$  to  $16^{\circ}02'N$ , disappearing in two locations: beneath the axial volcanic mound at  $15^{\circ}50'N$  and from  $\sim 15^{\circ}58'$  to  $16^{\circ}01'N$  (Figures 3a and 7 and Plate 2). The absence of

a detectable AMC beneath the volcanic mound is likely due to imaging problems associated with the rough seafloor topography. A stack limited to the near-offset traces of the CMP gathers for cross-axis line 1349 shows a very faint event at similar depths to the AMC event away from the volcanic mound. However, the second disruption at  $15^{\circ}58'-16^{\circ}01'$  cannot be attributed to rough topography. No event can be detected along cross-axis line 1346 or on either along-axis line through this area (Figures 3a, 3b, and 7 and Plate 2). North of this disruption, a short AMC event extending only 3 km along the axis is observed on both lines 1334 and 1347.

In addition to these locations where the AMC disappears for several kilometers the AMC event is weak and disrupted in two locations along line 1334 (Figure 3a): from  $15^{\circ}51'-15^{\circ}57'N$ , directly north of the axial volcanic mound, and from  $\sim 15^{\circ}35'$  to just south of the  $15^{\circ}38'N$  deval. At both locations a bright AMC event is detected on adjacent along-axis lines (1347 and 1348, respectively, Figures 3b and 3c). Presumably, the weak disrupted nature of the AMC beneath line 1334 reflects crossing a low-melt region of the melt lens or the lens edge.

The AMC lies at a shallow and quite uniform depth of  $1476 \pm 107$  m (average depth for line 1334, Table 5 and Figure 7) beneath the axial region of the southern segment. Beyond the axial summit trough the AMC is, on average, deeper and lies at a greater range of depths (Plate 2). The variations in AMC depth at this segment (total range close to 1000 m) are much greater than those of the overlying seafloor ( $<100$  m, away from segment ends).

The average width of the AMC measured from all cross-axis lines is  $1331 \pm 338$  m (Tables 2 and 5). The AMC is widest within the broad central part of the ridge. AMC widths for this segment are greater than average widths observed elsewhere on the EPR (Table 5), although well within the total range previously reported ( $4000$  to  $<500$  m [Kent et al., 1994]).

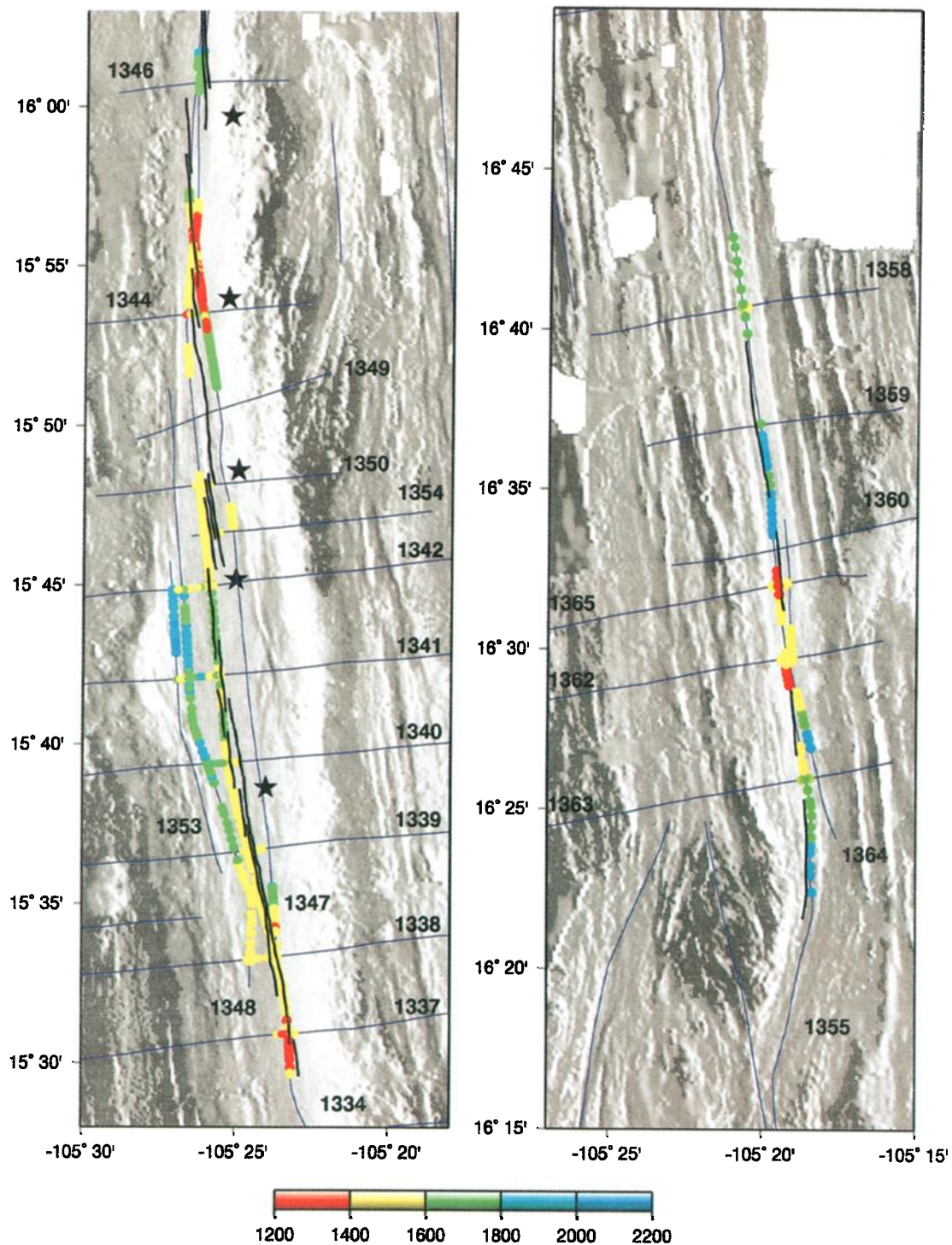


**Plate 2.** Depth to the AMC reflector picked from each along- and cross-axis line overlaid on shaded relief bathymetry of Plate 1. Color changes are every 200 m. AMC depths are calculated incorporating structure of layer 2A along each line and assuming crustal velocities given in Table 1. Note the good agreement between depths at line crossings (except for lines 1342 and 1365, where mismatches may reflect three-dimensional effects associated with imaging magma lens edge, see text). On along-axis lines where two lenses overlap in depth (at  $\sim 15^{\circ}54'$ ,  $15^{\circ}45'$ , and  $15^{\circ}42.5'N$ ), depth to the shallower lens is plotted in smaller dots on top of the deeper lens. The axial summit trough (AST) is shown in thin black line, and devals are indicated with black stars. Along the southern segment all devals are associated with changes in the AMC event (see text). The AMC is widely distributed beneath the southern segment at a range of depths but is shallowest centered beneath the narrow summit trough. Along the northern segment a narrower AMC is found which shoals and broadens beneath the shallowest untectonized portion of the ridge at  $\sim 16^{\circ}29'N$ .

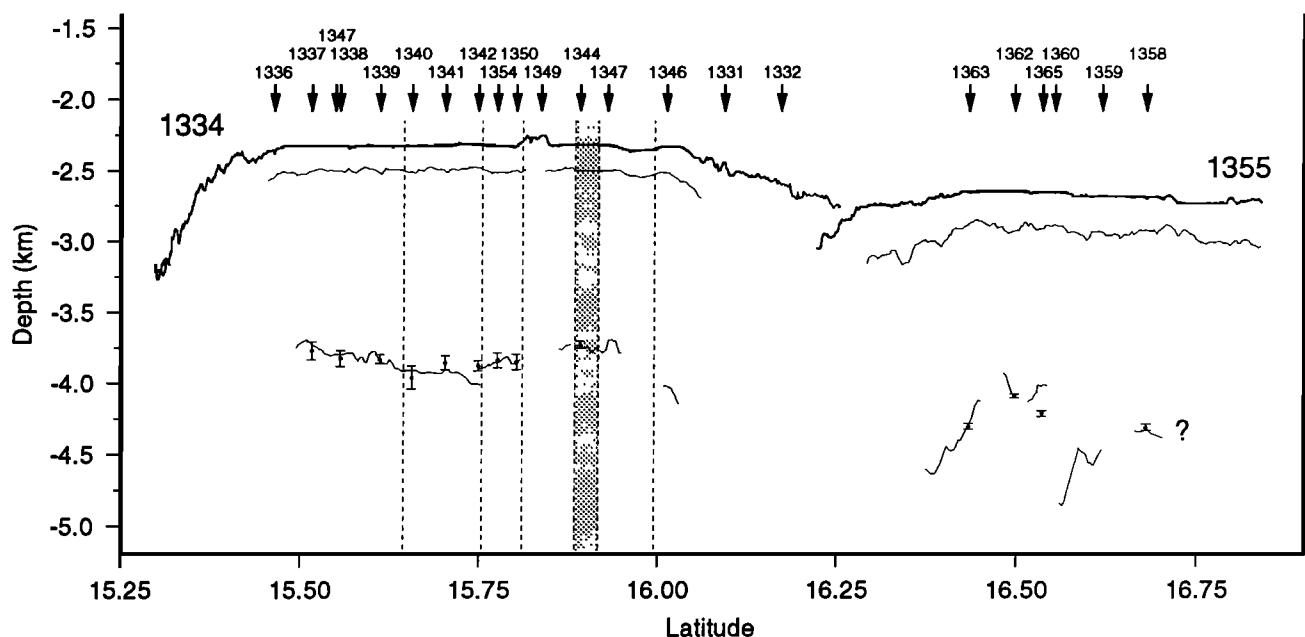


**Figure 7.** Line drawing interpretation of along-axis profiles 1334 and 1355 (Figures 3a and 3d) showing depth to seafloor, base of layer 2A, and AMC reflector. The location of a faint and weak possible AMC event at the northern segment is indicated with question mark. Line crossings are shown with labeled arrows, and average AMC depths from cross-axis lines (Table 2) are shown in heavy lines. Dashed vertical lines show locations of devals. The extent of the 15°53'-55'N deval is shaded. Along the southern segment the AMC is observed beneath much of the innermost axial zone with little variation in depth. North of the deval at 15°59'N, an isolated and deeper AMC event ~3 km long is observed. Layer 2A is markedly uniform in thickness along the axis of the southern segment, thickening slightly beneath the volcanic mound at 15°50'N and toward the segment ends. Along the axis of the northern segment the AMC is discontinuous, several hundred meters deeper on average, and more variable in depth than beneath the southern segment. Layer 2A is thicker on average and more variable in thickness.

#### 4.2. Segmentation of the AMC Reflector

In three locations along the southern segment, cross- and along-axis lines show disruptions in the AMC event where the AMC abruptly steps to a deeper level. In along-axis data the deeper reflection extends beneath the shallower one for up to 2 km giving rise to what appear to be multiple AMC reflections in these parts of the sections. The northernmost occurrence is located at 15°54'N and is imaged along lines 1347 and 1344 (Figure 5). Cross-axis line 1344 shows two AMC events offset by 100-150 ms with the deeper event to the east. At the same location, along-axis line 1347 shows two AMC events offset by 100 ms with the deeper event to the southeast clearly extending beneath the shallower one. Interestingly, in the vicinity of the overlapping AMC events the shallower event becomes discontinuous, composed of three segments each <1 km long. Lateral variations in layer 2A thickness account for some but not all of the travel time offset in the AMC event observed on these sections. Incorporating 2A thickness variations, the separation between the two AMC events is ~250-300 m with good agreement on both lines (Plate 2).

Multiple AMC events are also observed at 15°45' along lines 1334 and 1342 and at 15°41'-42'N along lines 1348 and 1341 (Figures 3 and 4 and Plate 2). Both of these occurrences are within the broadest part of the ridge axis and are associated with what appears to be a second discrete AMC lens located beneath the western half of the axis. Lines 1348 and 1353 show that the AMC underlying the western half of the plateau diminishes in

amplitude and disappears north of 15°45'N (Figure 3 and Plate 2). Notably, no AMC is imaged beneath the eastern half of the axis in this region.

Seismic imaging limitations could contribute to the multiple and step-like discontinuities we observe in the AMC event. For example, scattering from out-of-plane features can create coherent events in reflection data that may be incorrectly interpreted [e.g., Kent *et al.*, 1997]. Kent *et al.* [1993a] imaged a bright dipping reflector along a seismic line through the overlap basin of the 9°N OSC which was similar in depth to the AMC event observed elsewhere in their survey. Using Kirchhoff-Helmholtz synthetics, Kent *et al.* [1993a] conclude that scattering from a magma lens located 3-4 km away could plausibly account for the reflector they imaged through the OSC basin. Without three-dimensional (3-D) seismic coverage or detailed modeling, we cannot rule out the possibility that similar out-of-plane effects contribute to the multiple AMC events imaged within our survey area (e.g., lines 1347 and 1348). However, the good agreement between along and across-axis data at these occurrences of multiple events, the lack of any visible difference in the frequency character of the overlapping AMC reflections, and the observation that where multiple lenses are imaged they do not systematically come in at greater travel times than the AMC event on adjacent lines (e.g., on line 1348, of the two lenses observed at ~15°42'N the shallower lens lies at the same depths as the magma lens imaged over 1.5 km to the east on line 1334) give us confidence that these multiple events are not "sideswipe" artifacts.

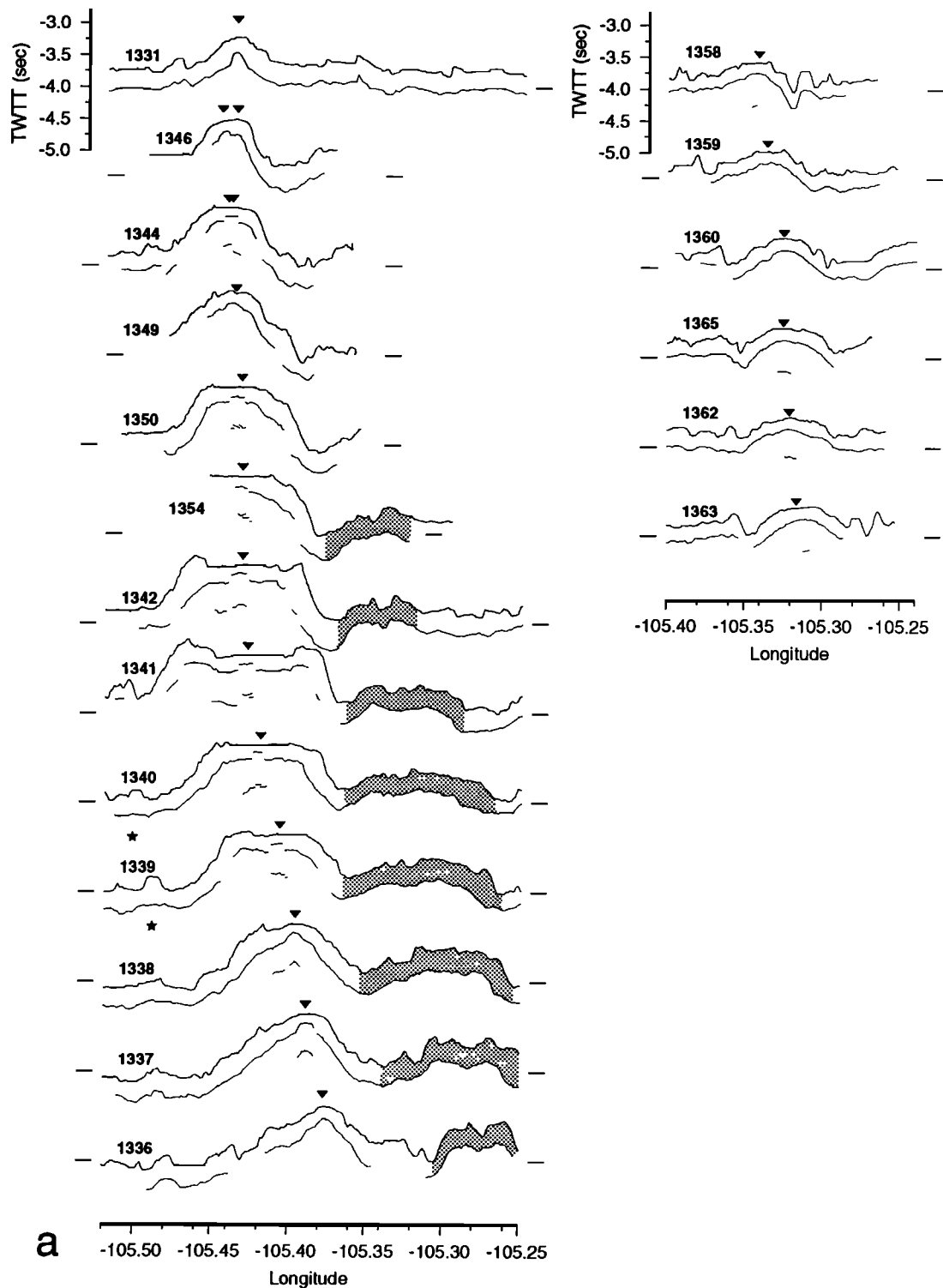


**Figure 8.** (a) Line drawing interpretations of cross-axis profiles showing two-way travel time (TWTT) to seafloor (from Hydrosweep data), base of layer 2A, and AMC. Profiles are arranged from south (bottom) to north (top) for the (left) southern and (right) northern segments. Horizontal lines at edges of profiles indicate 4.0 s. Small arrow points show location of AST where present or the shallowest point on the axial high. Stars indicate examples of local thickening of layer 2A beneath small volcanic cones within the west flank seamount field on the southern segment. Former ridge location on the east flank is shaded. The geometry of layer 2A along the southern segment is very different from that observed elsewhere along the EPR (see text). Toward the ends of the southern segment and beneath the northern segment, layer 2A attains close to its full thickness at zero age with minor thickening occurring within 1-2 km of the axis. (b) Layer 2A thickness in meters for portions of profiles shown in Figure 8a. Horizontal lines at edges of profiles indicate 400 m. Dashed lines correspond with regions where 2A is not imaged (shown as gaps in Figure 8a). Dots show picks for extent of the 2A accumulation zone given in Table 3. Note the local increase in layer 2A thickness along the eastern edge of the former ridge location. Similar asymmetric accumulation of layer 2A is also seen beneath the current axial plateau.

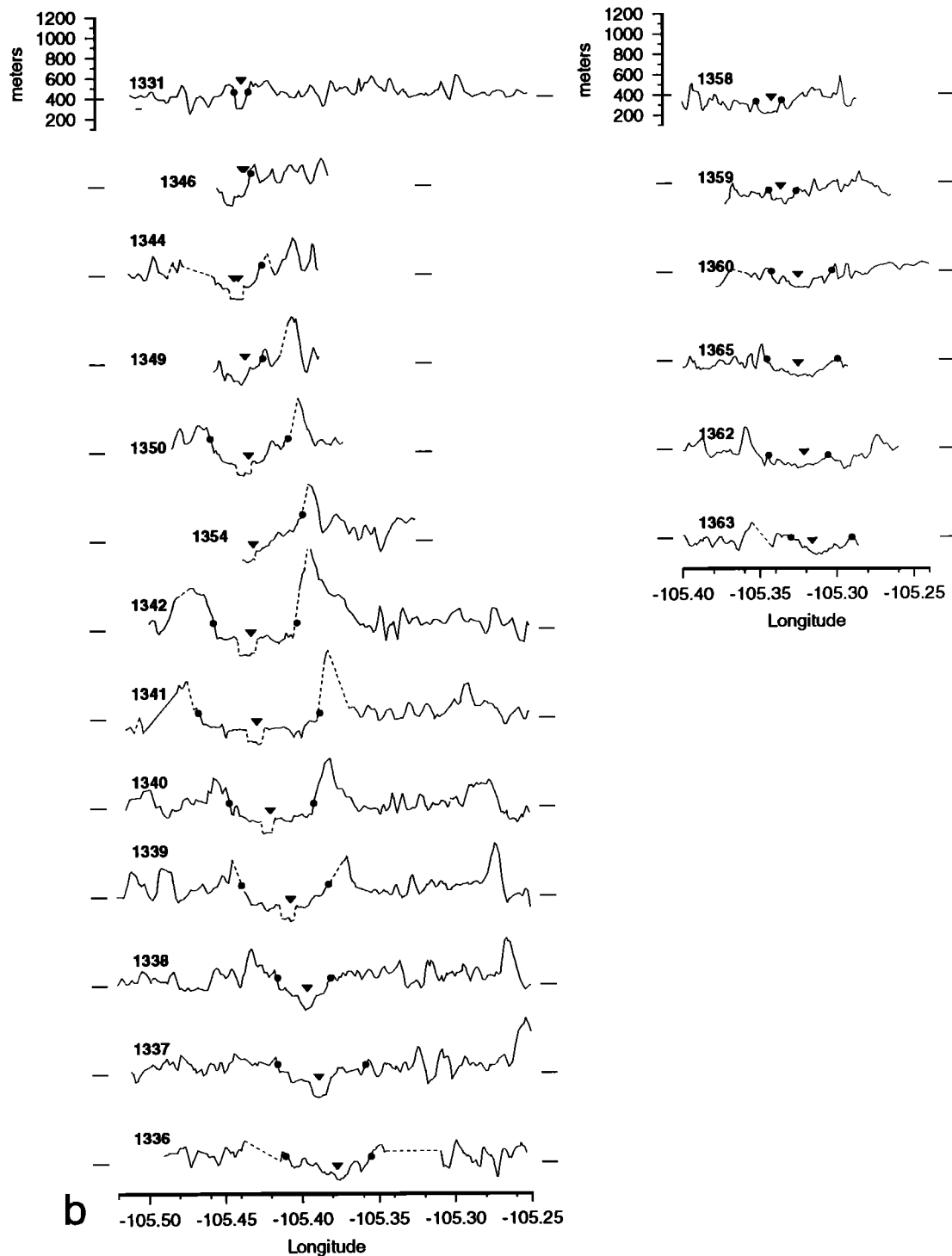


**Figure 8.** (continued)

Another imaging problem that must be considered is that the discontinuous magma lenses we image at different levels in the crust (e.g., Figures 4 and 5, lines 1341 and 1344) might actually be continuous through a steeply dipping region that we are unable to resolve. This possibility is unlikely for several reasons. Unmigrated sections show diffraction hyperbolae associated with both AMC events indicating edges to both features (Figure 4, line 1341). Secondly, we do successfully image comparably steep dips at the base of layer 2A (Figure 8). In addition, if these magma lenses were actually connected, it is difficult to envision how melt could remain at the deeper level. Pressure gradients should favor

rapid migration of melt within a connected lens to the shallower levels.

Cross-axis lines where two AMC events are imaged show that the break in the magma lens events roughly coincides with a rapid increase in layer 2A thickness, and imaging difficulties associated with these rapid lateral velocity changes are likely to be important. Clearly, some of the travel time difference between the magma lenses on these lines is due to the rapid change in the thickness of the low-velocity layer 2A. However, in addition to velocity "pull-up" where 2A is thin, rapid changes in layer 2A thickness may significantly distort hyperbolae associated with the

**Table 2. AMC Properties**

Line	Width of AMC, <sup>a</sup> m	Minimum AMC Depth, m	Average AMC Depth, <sup>a, b</sup> m
<i>Southern Segment</i>			
1336	-	-	-
1337	1100	1361	1446 (±67)
1338	1125, 800	1413	1491 (±59), 1524 (±22)
1339	1163	1440	1488 (±31)
1340	1700	1520	1637 (±83)
1341	675, 850	1534	1540 (±51), 1696 (±109)
1342	713, 775	1518	1561 (±37), 1583 (±58)
1354	1000	1459	1512 (±54)
1350	1025	1460	1535 (±52)
1349	-	-	-
1344	550, 500	1395	1412 (±25), 1729 (±44)
1346	-	-	-
1331	-	-	-
<i>Northern Segment</i>			
1363	488	1624	1652 (±23)
1362	725	1427	1445 (±16)
1365	1000	1561	1579 (±20)
1360	-	-	-
1359	-	-	-
1358	250	1595	1623 (±25)

Errors are ±75m for AMC width and ±50m for minimum and average AMC depth.

<sup>a</sup>Where two discrete lens events are imaged, the value for the lens located under the AST is given first.

<sup>b</sup>One standard deviation is given in parentheses.

AMC reflections, making it difficult to properly image the magma lens with poststack techniques. Improved images may be obtained with prestack methods that are designed for imaging structure with large lateral variations. However, we emphasize that offset lenses are observed where there is little change in layer 2A (e.g., line 1347).

Finally, the limitations of 2-D imaging clearly 3-D features must be considered. Lateral resolution of AMC structures is limited by the Fresnel zone which for our imaging source and magma lens depths is ~1000 m [Ponce-Correa *et al.*, 1999]. Migration improves lateral resolution and, in an ideal case, can reduce Fresnel zones to a quarter of the seismic wavelength at the target depths. For 2-D data this improvement is achieved in the in-profile direction but not across profile, where structure is assumed to extend infinitely. Three-dimensional seismic surveys of these sites of multiple AMC events would enable these underresolved structures to be adequately imaged, as well as permit correct processing of reflected or scattered energy from out-of-plane structures, both on the seafloor and within the crust.

#### 4.3. Northern Segment

Along the northern segment the AMC reflection is discontinuous, with several discrete events apparent in the combined along-axis data set (lines 1355 and 1364), each ~5-10 km long and located at different depths beneath the seafloor (Plate 2 and Figure 7). The northernmost AMC is very faint on along-axis line 1355 but is a clear diffractive event on the stacked section of cross-axis line 1358. The southernmost events shoal to the north. Changes in layer 2A structure are well imaged along this segment and do not account for the changes in AMC depth.

However, variations in the location of the survey track with respect to the AMC lens clearly account for some of the variability in AMC depth and presence. For example, AMC reflections are detected on along-axis line 1364 around 16°30'N, where none are imaged on line 1355 located only 500 m to the west. Furthermore, sideswipe effects associated with along-strike imaging of a narrow AMC likely contribute to the dipping nature of the southernmost AMC events (e.g., along line 1364 at ~16°27'N).

Within the innermost axial region of this segment the AMC lies at an average depth of 1684 ±236 m, with a total depth range of 900 m (measured from line 1355). The average depth from cross-axis data is considerably less (1552 ±87 m, Table 5), which may reflect location of these lines primarily where along-axis data show the lens is shallow. The AMC locally shoals beneath the shallowest part of the ridge centered at 16°30'N where the axis appears untectonized (Plate 2). The AMC is also widest in this region. The average width of the AMC from cross-axis data is 616 ±321 m (Table 5), less than half the average width for the southern segment.

**Table 3. Layer 2A Thicknesses and Width of 2A Accumulation Zone**

Line	On-Axis 2A Thickness, <sup>a</sup> m	Average 2A Thickness Outside 2A Accumulation Zone, <sup>b, c</sup> m	Width of 2A Accumulation Zone, <sup>d</sup> km
<i>Southern Segment</i>			
1336	237	470 (±75)	6.1
1337	177	463 (±92)	6.2
1338	166	463 (±84)	4.1
1339	164	503 (±106)	6.1
1340	160	426 (±86)	6.1
1341	169	452 (±77)	8.4
1342	157	444 (±84)	5.9
1354	-	527 (±92)	7.0 <sup>e</sup>
1350	202	522 (±54)	5.5
1349	197	425 (±84)	5.4 <sup>e</sup>
1344	173	510 (±109)	3.9 <sup>e</sup>
1346	225, 315 <sup>f</sup>	526 (±71)	3.2 <sup>e</sup>
1331	313	448 (±65)	1.1
<i>Northern Segment</i>			
1363	253	411 (±83)	4.4
1362	238	398 (±82)	4.3
1365	246	405 (±61)	4.9
1360	252	400 (±71)	4.3
1359	253	336 (±61)	2.0
1358	223	351 (±74)	1.8

Estimated errors are ±30m for on-axis and average thicknesses and ±0.3km for accumulation zone width.

<sup>a</sup>Values correspond with thickness beneath the AST where present or shallowest point of axial high.

<sup>b</sup>One standard deviation is given in parentheses.

<sup>c</sup>For the southern segment, averages exclude thicknesses associated with the former ridge location on the east flank.

<sup>d</sup>Layer 2A accumulation zone is defined as region over which 2A thickens to the average value on the ridge flanks from Table 4.

<sup>e</sup>The entire 2A thickening zone is not imaged on these lines, and estimates given correspond to twice the observed half width.

<sup>f</sup>Values are measured beneath both AST lineations of the 15°59'N devial.

**Table 4.** Layer 2A Characteristics for Axial Region of Southern Segment

Line <sup>a</sup>	On-Axis 2A Thickness, <sup>b</sup> m	Width of Region of Thin 2A Beneath AST, m	Average 2A Thickness Within Thin 2A Zone Beneath AST, <sup>c</sup> m	Average 2A Thickness Beneath Rest of Axial Plateau, <sup>c, d</sup> m
1337	177	738	191 (±11)	341 (±37)
1338	166	500	181 (±18)	339 (±32)
1339	164	663	181 (±15)	331 (±43)
1340	160	788	159 (±5)	324 (±41)
1341	169	850	172 (±14)	318 (±44)
1342	157	875	162 (±10)	332 (±25)
1354	-	-	-	408 (±71)
1350	202	775	196 (±11)	389 (±85)
1349	197	650	236 (±31)	391 (±82)
1344	173	800	171 (±3)	321 (±40)
1346	225, 315	675	240 (±19)	341 (±32)

Errors are ±30m for on-axis thickness and both average thicknesses and ±150m for width of region of thin 2A beneath AST.

<sup>a</sup>Only lines crossing the flat plateau portion of the segment are included.

<sup>b</sup>From Table 3.

<sup>c</sup>One standard deviation is given in parentheses.

<sup>d</sup>Region of thin 2A centered beneath AST is excluded.

## 5. Observations: Geometry of Seismic Layer 2A

### 5.1. Southern Segment

Along the southern segment, layer 2A is thinnest within the innermost axial zone and varies little in thickness along strike (average thickness for line 1334 measured away from segment ends is 170 ±44 m, Figure 7 and Table 5). The primary exception is a local increase (of ~30 m) beneath the axial volcanic mound at 15°50'N (observed on lines 1349 and 1350, Table 3). Zero-age thicknesses increase toward the ends of this ridge segment north of the 15°59'N deval.

Cross-axis lines show that where there is a flat plateau, layer 2A remains uniformly thin for a region ~750 m wide (Table 4), located beneath the AST and roughly centered above the AMC reflector (Figure 8). Where a second AMC event is observed, the region of thin 2A overlies the shallowest reflector (Figures 4, 5, and 8, lines 1341, 1342, and 1344). At the edges of this uniform thin zone, layer 2A increases in thickness abruptly over a region as narrow as 100-300 m (inferred from CMP gathers). Layer 2A is approximately constant in thickness (350 m) beneath the rest of the flat-topped axial plateau thickening to 500-700 m at the plateau edges (within 1.5 to 5 km of the AST, Figure 8b). Thicknesses on the east side of the plateau are greater than those on the west (accumulations exceed 750 m compared with average thicknesses of ~550 m to the west). The greatest accumulations found in the survey area underlie the split seamount located at 15°40'-47'N on the plateau edges, consistent with volcanic construction of this edifice. Toward the ends of the ridge segment the abrupt step in layer 2A within the inner zone is not observed. Here layer 2A thickens gradually beneath the axial high over a narrow region and does not reach the large thicknesses observed within the central part of the segment (e.g., Figure 8, lines 1336 and 1331, and Table 3). This accumulation pattern is much more typical for the EPR [e.g., Kent et al., 1994; Carbotte et al., 1997;

Hooft et al., 1997] than the double-step pattern imaged to the south.

The ridge flanks are dominated by short wavelength variations in layer 2A thickness, presumably associated with abyssal-hill-forming processes [e.g., Harding et al., 1993; Carbotte et al., 1997], with average 2A thicknesses of 450-525 m (Table 3 and Figure 8). Local increases in 2A thickness are observed beneath small volcanic cones associated with the Mudskipper seamount chain (e.g., lines 1339 and 1340, Figure 8). The base of layer 2A is approximately horizontal beneath these cones, suggesting volcanic construction on top of the preexisting extrusive layer without deflection of the base of this layer due to loading. Larger accumulations of layer 2A are found along the eastern edge of the former axial ridge than along the western edge (>550 m compared with ~450 m, Figure 8), similar to the asymmetric pattern of accumulation beneath the current axial plateau. There is no linear zone of thin layer 2A beneath the former ridge, analogous to that which characterizes the innermost zone of present-day accretion along the southern segment.

In this study we identify the layer 2A accumulation zone as the region over which 2A thickens to its average value on the ridge flanks (Table 3). This definition provides a minimum estimate of accumulation zone width at the southern segment on the assumption that total 2A thicknesses at the edges of the neovolcanic zone for the present-day spreading center are likely to be at least as large as those on the adjacent ridge flanks. We choose this definition rather than the width of the zone of maximum thickening as the very large 2A thicknesses found along the plateau edges are likely to be associated with the recent ridge jump to this location (see section 6). Following this definition, we measure a wide accumulation zone ranging from 5 to 8 km about the AST (Table 3, Figure 8b) for most of the southern segment, within which layer 2A approximately triples in thickness. At the northern end of this segment, less thickening is observed (increases over zero-age thicknesses of a factor of 1.5 to 2) over a narrower zone only 1-3 km wide.

### 5.2. Northern Segment

The average thickness of layer 2A along the axis of the northern segment is 270 ±72 m (line 1355), ~60% thicker than for the southern segment. Minor accumulation of layer 2A occurs gradually beneath the axial high with average thicknesses of 350-400 m on the ridge flanks (Table 3). The width of the 2A accumulation zone (2-5 km) is narrower than observed for most of the southern segment. The greatest widths are found within the shallowest part of this segment, the accumulation zone narrowing beneath the more tectonized axis to the north. Although our data coverage is limited, it appears that 2A thicknesses on the ridge flanks are lower within the northerly part of the segment. (Table 3 and Figure 8).

## 6. Discussion

In sections 6.1-6.3 we discuss implications of our study for questions regarding the influence of magma supply on the characteristics of the magma lens and the extrusive layer and the relationship between tectonic and magmatic segmentation of the ridge.

### 6.1. What is the Influence of Magma Supply on Magma Lens Characteristics?

Phipps Morgan and Chen [1993a, b] present models for crustal accretion which predict systematic variations in the depth

**Table 5.** Comparison of AMC and Extrusive Layer Characteristics Along the EPR

Area	Average Layer 2A Thickness On Axis in Two-Way Travel Time, <sup>a</sup> sec	Average Layer 2A Thickness On Axis, <sup>a</sup> m	Average AMC Depth, <sup>a</sup> m	Average AMC Width, <sup>a</sup> m
<b>Southern segment</b>				
Cross-axis lines <sup>b</sup>	0.142 (±0.016)	195 (±22)	1456 (±61)	1331 (±338)
Along axis line 1334	0.124 (±0.032)	170 (±44)	1476 (±107)	-
<b>Northern segment</b>				
Cross-axis lines <sup>b</sup>	0.177 (±0.01)	243 (±12)	1552 (±87)	616 (±321)
Along axis line 1355	0.196 (±0.052)	270 (±72)	1684 (±236)	-
<b>13°N</b>				
Cross-axis lines <sup>c</sup>	0.181 (±0.013)	261 (±18)	1334 (±134)	496 (±185)
<b>9-10°N</b>				
Cross-axis lines	0.125 (±0.027) <sup>d</sup>	172 (±37) <sup>d</sup>	1524 (±105) <sup>e</sup>	1186 (±1346) <sup>e</sup>
<b>14°S</b>				
Cross-axis lines	0.168 (±0.02) <sup>f</sup>	220 (±26) <sup>f</sup> 243 (±29) <sup>g</sup>	1095 (±107) <sup>g</sup>	660 (±205) <sup>g</sup>
Along axis line	-	180 (±60) <sup>h</sup>	1087 (±78) <sup>h</sup>	-
<b>17°S</b>				
Cross-axis lines	0.117 (±0.02) <sup>i</sup>	153 (±26) <sup>i</sup>	1135 (±154) <sup>g</sup>	802 (±311) <sup>g</sup>
Along axis line	0.142 (±0.013) <sup>j</sup>	186 (±17) <sup>j</sup>	1196 (±73) <sup>j</sup>	-

Along-axis data provide dense and extensive areal coverage but can include apparent depth variations due to ship wander relative to the innermost axis. Cross-axis lines permit identification of innermost axis but only provide data at sparse intervals of 5-10 km and are spatially biased to shallower portions of ridge segments.

<sup>a</sup>One standard deviation given in parentheses.

<sup>b</sup>Average values are computed from Tables 1 and 2. Where two AMC events are observed on one line, the combined width of both events is used.

<sup>c</sup>From *Babcock et al.* [1998].

<sup>d</sup>Measured by S. M. Carbotte from *Harding et al.* [1993] and converted to depth using same velocity function as used for this study.

<sup>e</sup>From *Kent et al.* [1993b]. Average includes wide AMC at 9.31°N.

<sup>f</sup>Measured by S. M. Carbotte from *Kent et al.* [1994] converted to depth using ESP data of *Detrick et al.* [1993].

<sup>g</sup>From *Hooft et al.* [1997].

<sup>h</sup>From *Tolstoy et al.* [1997]. Estimates are obtained from wide aperture profile data.

<sup>i</sup>From *Carbotte et al.* [1997] converted to depth using ESP data of *Detrick et al.* [1993].

<sup>j</sup>From *Mutter et al.* [1995] converted to depth using ESP data of *Detrick et al.* [1993].

of the magma lens with spreading rate and magma supply. In these models, lens depth is controlled by the thermal structure of the ridge axis, which reflects the balance between heat input to the crust through magma injection and heat removed through hydrothermal circulation. These models predict that for constant spreading rate a shallower lens will be associated with greater magma supply to a ridge segment.

In Figure 9 and Table 6 we examine the relationship between magma lens and extrusive layer characteristics and commonly used morphological indicators of magma supply (axial depth and cross-sectional area [e.g. *Scheirer and Macdonald*, 1993]). These comparisons show a weak relation between axial depth and lens depth with a somewhat shallower lens underlying the southern segment (Figure 9 and Table 6). A stronger positive correlation is observed between lens width and axial morphology, with a magma lens that, on average, is twice as wide as beneath the shallow and broad southern ridge. Along the narrow deep northern segment the lens systematically shoals and widens

beneath the shallowest untectonized part of the segment (Plate 2 and Figure 8). The correlation between magma lens characteristics and axial morphology that we obtain is much stronger than that reported by *Hooft et al.* [1997] for data from the southern EPR (correlation coefficients of <0.1-0.3 for lens depth and width compared with axial depth and area, see their Table 2). The differences between our study and that of *Hooft et al.* [1997] may reflect lack of resolution in this previous work due to the modest contrasts in magma budget represented by the regions imaged. The cross-axis seismic data compared by *Hooft et al.* [1997] were collected primarily in areas of presumed robust supply (14°S and 17°S) where the likelihood of imaging a magma lens was assumed to be greatest.

However, superimposed on the segment-scale relationship between lens characteristics and axial morphology are large local variations that are not simply related to morphology (Figure 9). In spite of the pronounced contrasts between the two segments the AMC is found at the same wide depth range (~1300-2200 m),

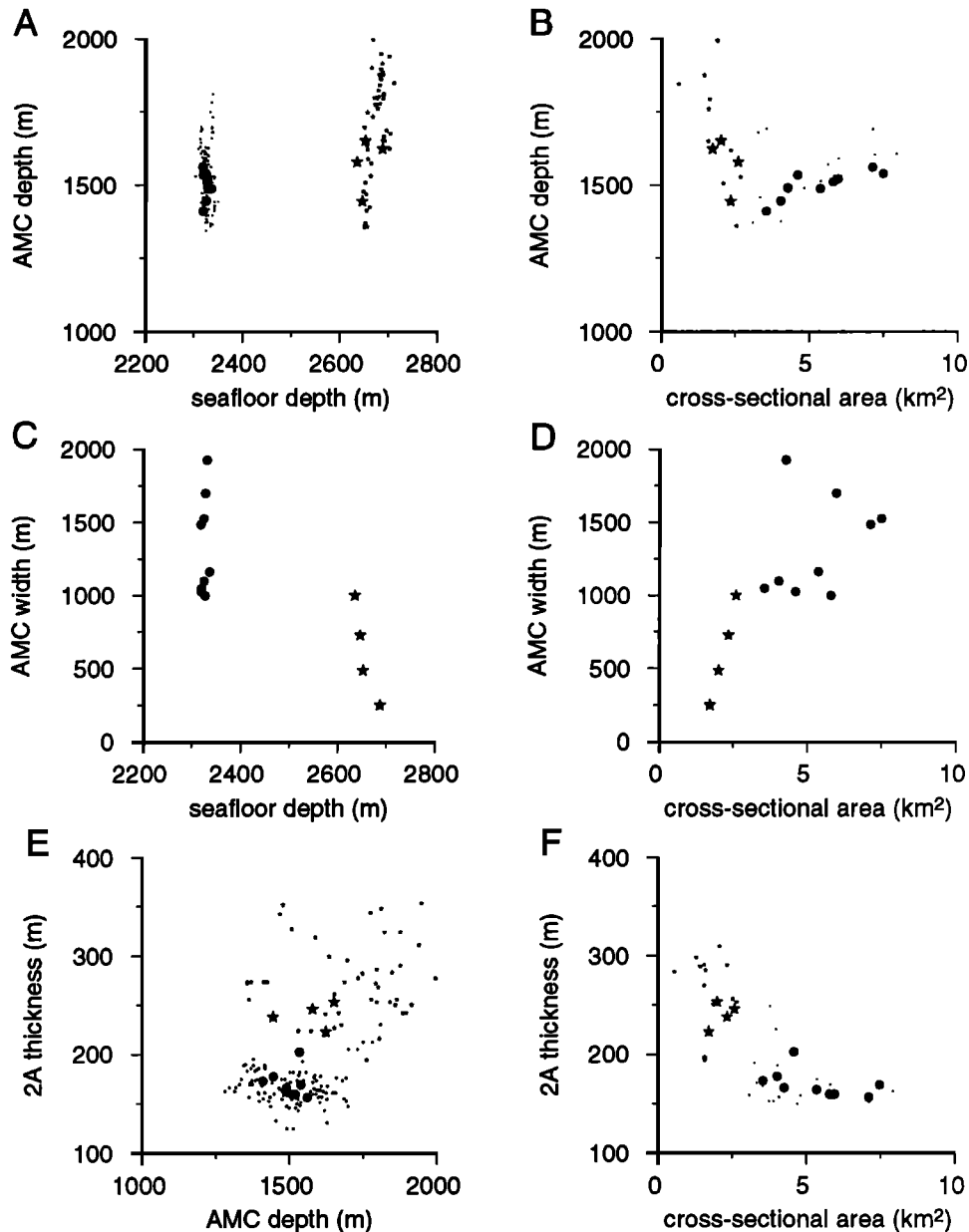


**Figure 9.** Plots showing relationships between morphological indicators of magma supply (seafloor depth and cross-sectional area) (a-d) and magma lens depth and width, (f) and layer 2A thickness on axis. Stars show data from the northern segment, and circles show data from the southern segment. Large symbols are used for cross-axis data and, small symbols are used for along axis data. Layer 2A thickness on axis is plotted versus AMC depth in Figure 9e. Correlation coefficients for these relationships are given in Table 6.

with minimum AMC depths as shallow at the northern segment as at the southern. Furthermore, at both segments only minor changes in the elevation of the seafloor are observed where the underlying AMC varies in depth by  $\sim 1$  km. At the southern segment the AMC varies in width over a wide range, and no systematic trend with morphology is evident.

Hussenoeder *et al.* [1996] and Hooft *et al.* [1997] suggest that magma lens characteristics are closely related to dike injection and eruption events which, at fast spreading rates, likely occur on short timescales of 10 to 100 years. Our data are consistent with this hypothesis. Seafloor observations show that the zone of present-day volcanic and hydrothermal activity is largely concentrated within the narrow AST [Macdonald and Fox, 1988;

Haymon *et al.*, 1991]. The region of thinnest layer 2A at the ridge axis locates the longer-term locus of active crustal creation (1 kyr to, perhaps, several kyr). Along the southern Orozco segment the seismically inferred extrusive layer is thinnest beneath the AST and above where the magma lens is shallowest (Figure 8). In places where a second, deeper magma lens is imaged, there is no summit trough in the overlying seafloor or corresponding region of thin layer 2A. These relationships imply that crustal creation is focused where the magma lens is shallowest and that AMC depth is closely associated with eruption processes. Magma lenses may be dynamic features residing at different levels beneath a segment and with varying widths depending on local variations in both magma delivery to the lens from the mantle below as well as

**Table 6.** Correlation Coefficients for Ridge Morphology and Crustal Structure

	Seafloor Depth	Cross-sectional Area <sup>a</sup>	AMC Width	AMC Depth	On-Axis Layer 2A Thickness	Width of Layer 2A Accumulation Zone
<i>Across-Axis Lines</i>						
Seafloor depth	1.00	0.78	0.75	0.53	-0.65	0.57
Cross-sectional area <sup>a</sup>	0.78	1.00	0.73	-0.18	-0.67	0.72
AMC width	0.75	0.73	1.00	-0.36	-0.72	0.53
AMC depth	0.53	-0.18	-0.36	1.00	0.47	-0.26
On-axis 2A thickness	0.65	-0.67	-0.72	0.47	1.00	-0.69
Width of 2A accumulation zone	0.57	0.72	0.53	-0.26	-0.69	1.00
<i>Along-axis Lines 1334 and 1355</i>						
Seafloor depth	1.00	0.81	-	0.59	-0.86	-
Cross-sectional area <sup>a</sup>	0.81	1.00	-	-0.33	-0.74	-
AMC depth	0.59	-0.33	-	1.00	0.51	-
2A thickness	-0.86	-0.74	-	0.51	1.00	-

<sup>a</sup>From Scheirer and Macdonald [1993].

magma removal by dike intrusion and eruption. Magma supply may contribute to the regional depth and width of the lens beneath a ridge segment, but these parameters are strongly modulated within a segment by local eruption processes.

## 6.2. Does Magma Supply Influence Emplacement of the Extrusive Layer?

Harding *et al.* [1993] suggests that the thickness of layer 2A may reflect magma supply to the ridge with greater accumulations where magma supply is enhanced. Our data indicate a more complex relationship. On axis we obtain good negative correlations between layer 2A thickness, axial depth, and cross-sectional area (Table 6 and Figure 9), with thinner 2A along the shallow and broad southern segment. Layer 2A thickens toward the ends of the ridge segments (Table 3 and Figure 7), as is observed elsewhere along the EPR [e.g., Hooft *et al.*, 1997; Detrick *et al.*, 1993]. Unaccounted changes in upper crustal velocities associated with, for example, increased fracturing and hydrothermal circulation could contribute to this inverse relationship between morphology and layer 2A thickness on axis. However, an implausible reduction in *P* wave velocities for layer 2A would be required to account for the full range of 2A thickness observed (from values within the reported range from refraction studies of ~2.5-3 km/s to velocities similar to or lower than that of water).

Buck *et al.* [1997] propose that the thickness of extrusives which can accumulate on axis reflects the influence of magma pressure within the melt lens. In their model, Buck *et al.* [1997] assume that eruption of magma will occur when the average density of the intrusive and extrusive section overlying the magma lens is greater than magma density. However, ongoing eruption will thicken the low-density extrusive layer, decreasing the average density of the overburden and hence the magma pressure within the magma lens, thereby inhibiting further eruption. This process will give rise to an equilibrium thickness for the extrusive layer above a magma lens of given depth and predicts that a thicker extrusive layer can accumulate at ridges with a deeper melt lens. The weak positive correlation we observe between magma lens depth and on-axis extrusive layer thickness (Figure 9 and Table 6) provides some support for this model.

Away from the innermost zone the inflated southern segment is associated with greater accumulations of layer 2A and a wider

region of accumulation than found at the northern segment, indicating a direct relationship between axial morphology and the long-term accumulation of extrusives (Tables 3 and 6 and Figure 9). However, simple interpretation of the large accumulations along the plateau edges of the southern segment in terms of magma supply is complicated by the recent tectonic history of the region. As described in section 2.3, the southern ridge segment jumped to its current location within the past <100 kyr, and the duration of spreading at this site is confined to the axial high. Layer 2A thicknesses along the edges of the axial high (550 to >750 m) are greater than averages for the flanks of the southern segment (450-525 m), indicating that these accumulations are not typical of long-term accretion at this site (Figure 8 and Table 3). Buildup of layer 2A along the plateau edges could represent accumulation of volcanics on top of a preexisting extrusive layer following ridge jump to the current location. Alternatively, these large thicknesses could reflect recent increase in extrusive volcanism, presumably associated with tapping the melt source for the Mudskipper seamount chain. Interestingly, extrusive layer thickness is greater along the eastern than along the western edges of both the axial plateau and the former ridge location (Figure 8). This asymmetric accumulation could reflect small westward shifts in the locus of active eruption at both its current and former east flank site.

Along the northern segment, layer 2A acquires most of its thickness at zero age, and only minor thickening occurs within a 2-5-km-wide zone about the AST (increases of a factor of 1.5, Table 3 and Figure 8). A narrow accumulation zone is also observed at the ends of the southern segment, and little accumulation of lavas away from the innermost axis may typify regions of low magma supply. Both the width of the zone of dike injection and the typical distances lavas flow from their eruption site may control the geometry of the extrusive layer accumulation zone [Kent *et al.*, 1994; Hooft *et al.*, 1996; Carbotte *et al.*, 1997]. From modeling and seismic observations, Hooft *et al.* [1996] infer a narrow dike injection zone and predict that lava flow lengths play a dominant role in the extrusive layer emplacement zone. The distances that lavas flow must depend on magma and eruption characteristics such as lava viscosity, volume, eruption temperature, and effusion rate. So, for example, low effusion rates and more viscous lavas may give rise to pillow flows that do not extend significant distances from their eruption site, forming a narrow zone of extrusive accumulation. Hotter,

less viscous magmas forming sheet and lobate flows that can travel significant distances from their eruption site may be associated with the wide accumulation zone along the southern segment. Observations of flow lengths, morphology, and volume combined with geochemical studies can be made to directly evaluate the role of lava characteristics on the geometry of the extrusive layer accumulation zone. The width of the dike injection zone is more difficult to constrain although further near-bottom seismic and magnetic studies would provide important indirect evidence.

### 6.3. Tectonic and Magmatic Segmentation

Along the southern segment all devals identified from sidescan sonar data correspond with discontinuities or changes in the magma lens, indicating a genetic link between magmatic segmentation ~1.5 km below the seafloor and the finest-scale segmentation of the narrow axial depression. At the northernmost deval at 15°59'N the magma lens disappears, with a deeper, isolated AMC lens extending for only 3 km beneath the axis to the north. The AMC lens is offset to the east relative to the magma lens reflector to the south, as is the overlying AST. Preliminary results from a detailed geochemical sampling program carried out in fall 1997 show a marked difference in lava chemistry across this deval (C. Langmuir and J. Bender, personal communication, 1998), consistent with our findings of discrete magma lenses north and south of this discontinuity. At the 15°53'-55'N deval, two AMC events at different levels in the crust are observed, and it appears that separate magma lenses are associated with the adjoining fourth-order ridge segments. The deval at 15°48'N bounds the southern end of the volcanic mound, beneath which the magma lens cannot be detected. South of the 15°45'N deval, a magma lens is detected beneath the western half of the axial plateau, which cross-axis lines suggest is a distinct body from that underlying the AST (Plate 2 and Figure 8). Beneath the AST at this same location a small discontinuity in the AMC reflector is observed along line 1334. South of the 15°38'N deval, the AMC diminishes in amplitude on line 1334, and a break in the AMC is observed on adjacent line 1348 (Figure 3). Fine-scale tectonic segmentation is poorly defined along the northern segment. However, the magma lens may be segmented along this segment as well where a series of AMC events 5-10 km long are imaged roughly centered beneath the ridge axis.

Previous seismic studies show similar evidence for segmentation of the AMC coincident with the fine-scale tectonic segmentation of the ridge. *Kent et al.* [1993b] infer changes in the width of the AMC lens across devals at 9°17'N and 9°35'N. A seismic tomographic study in this same region shows a pinching/narrowing of the axial low-velocity volume (region of elevated temperatures underlying the AMC) beneath the 9°35'N and 9°28'N devals [Toomey *et al.* 1990, 1994]. At a prominent step in the AST located at ~8°50'N, two AMC events offset by ~100 m are imaged, similar to those we observe at 15°53'-55'N (see common depth profile 57 of *Kent et al.* [1993b]). *Babcock et al.* [1998] report depth and amplitude changes in the AMC event across devals at 12°46'N and 13°20'N.

Although correlation between magmatic and tectonic segmentation is apparent in these previous studies, the nature of the transition in the AMC reflector at devals is difficult to characterize in detail because of sparse data coverage. Our data coverage is better suited to address this question and provides a glimpse of the three-dimensional nature of the magma lens at devals. We find evidence that discrete magma lenses may be associated with individual ridge segments bounded by devals and

that transitions across devals can be abrupt. Beneath the innermost axial zone where active eruption is focused, magma lenses may lie at similar depths and, in some places, form a continuous body beneath devals within the resolution limits of seismic reflection imaging. However, away from this innermost zone, segmentation of the AMC lens becomes much more pronounced with the lens extending beneath different parts of the axial high and to different depths from one segment to the next.

*Langmuir et al.* [1986] conclude that the geochemistry of EPR axial lavas requires discontinuous magma chambers or magma chambers that are not well mixed laterally at scales comparable to the segmentation defined by devals. The close correspondence we observe between devals and discontinuities in the AMC event supports these inferences from petrologic studies.

Finally, the geometry of the magma lens beneath the broadest part of the ridge axis suggests influence of the nearby Mudskipper seamount chain. A magma lens is detected beneath the western half of the axial plateau extending to the rifted seamount at the plateau edge and sloping up toward the west. This magma lens appears separate from that underlying the AST, and no magma lens is found beneath the eastern half of the plateau. Magma lens geometry in this area may reflect modification of the thermal structure of the ridge axis associated with the melt source for the seamount chain, resulting in elevated temperatures within the shallow crust extending to the west. Alternatively, there may be hydraulic connection between the shallow magma plumbing for the ridge and the seamount chain. Recently collected geochemical data (C. Langmuir and J. Bender, personal communication, 1998) will help discriminate between these hypotheses.

## 7. Summary

On the basis of our combined bathymetric and multichannel seismic data set of the two contrasting segments of the EPR north of the Orozco fracture zone we find the following:

1. The southern ridge segment has experienced a complex recent tectonic history including a westward ridge jump of ~7-10 km within the past 100 kyr and rapid northward migration (~240 mm/yr) of a small ridge offset that now coincides with the deval at 15°59'N. These changes in ridge geometry presumably occurred in response to enhanced melt supply to the axial regime associated with increased proximity of the Mudskipper seamount chain. The former ridge axis location coincides with an 8-km-wide plateau located on the east flank which is similar in morphology and upper crustal structure to the current axis. At both locations, large accumulations of the seismically inferred extrusive layer are found preferentially along the eastern edges of these plateaus which may be associated with small-scale westward migration of the locus of active accretion. A transition from fast- to intermediate-spreading axial morphology occurs along the northern ridge segment where a shallowly rifted axial high develops north of 16°30'N.

2. Large-scale morphological characteristics of the two Orozco segments do provide some indication of magma lens characteristics with a lens which is, on average, twice as wide and 100-200 m shallower beneath the inflated southern segment and which systematically widens and shallows beneath the shallowest part of the northern segment. However, large local variations in both lens width and depth are also observed independent of morphological variations. We conclude that contrasts in magma supply inferred from axial morphology contribute to the width and depth of the magma lens from one ridge segment to the next but that within a segment, magma lens characteristics may be

strongly modulated by local processes of magma delivery and removal.

3. In the innermost axial zone a negative correlation between extrusive layer thickness and morphological indicators of magma supply is observed with a thicker layer accumulated along the deeper, narrow northern segment and toward ridge segment ends. In the region of active eruption and focused crustal creation located above the magma lens, extrusive thickness is likely governed by fundamental processes of magma eruption (e.g., magma pressure) and not by the volume of magma present or supplied to the region. A positive correlation between axial morphology and the extrusive layer accumulation zone is found with the extrusives more than tripling in thickness over a wide zone along most of the southern segment. At the northern segment and toward the north end of the southern segment, minor thickening of the extrusive layer is observed within a narrower region about the axis, and a narrow accumulation zone may typify regions of reduced magma supply.

4. Segmentation of the summit trough coincides with discontinuities or changes in the magma lens, with separate magma lenses associated with neighboring ridge segments bounded by devals. These individual sills may be connected beneath devals within the region of active eruption. However, away from this innermost zone, magma sills may extend to different depths, underlie different parts of the axial high, and, in some locations, interfinger at their adjoining edges such that lenses at different levels within the crust overlie one another. The close correspondence we observe between structural segmentation of the narrow axial depression and changes in the geometry of the magma lens located ~1.5 km below indicates a genetic link between devals and upper crustal magma plumbing.

5. The Mudskipper seamount chain has influenced the distribution of magma beneath the ridge axis with a second magma lens underlying the western half of the axial plateau where the seamount chain approaches the ridge. This magma lens geometry could reflect modification of upper crustal thermal structure due to proximity of the seamount melt source or hydraulic connection between the axial magma lens and the magma chamber for the seamount chain.

**Acknowledgments.** We thank the captain and crew of the R/V *M. Ewing* and the dedicated efforts of the whole scientific party for the success of cruise EW9503. We thank Peter Buhl and John Deibold for many valuable discussions regarding data processing and interpretation. Graham Kent, Emilie Hooft, and the associate editor provided careful reviews that improved the manuscript. This research was supported by NSF grants OCE 94-02171 and 98-11483 to S.M.C. This is Lamont-Doherty Earth Observatory contribution 5978.

## References

- Babcock, J. M., A. J. Harding, G. M. Kent, and J. A. Orcutt, An examination of along-axis variation of magma chamber width and crustal structure on the East Pacific Rise between 13°30'N and 12°20'N, *J. Geophys. Res.*, **103**, 30,451-30,467, 1998.
- Barth, G. A., and J. C. Mutter, Variability in oceanic crustal thickness and structure: Multichannel seismic reflection results from the northern East Pacific Rise, *J. Geophys. Res.*, **101**, 17,951-17,975, 1996.
- Bender, J., M. Cormier, C. Langmuir, S. Shirey, K. Donnelly, S. Carbotte, and PANRI Team, The East Pacific Rise and its flanks: New results between 15°N and 19°N, *EOS Trans. AGU*, Fall Meet. Suppl., **79** (45), F832, 1998.
- Buck, R. W., S. M. Carbotte, and C. Z. Mutter, Controls on extrusion at mid-ocean ridges, *Geology*, **25**, 935-938, 1997.
- Carbotte, S. M., and K. C. Macdonald, East Pacific Rise 8°-10°30'N: Evolution of ridge segments and discontinuities from SeaMARC II and three-dimensional magnetic studies, *J. Geophys. Res.*, **97**, 6959-6982, 1992.
- Carbotte, S. M., J. C. Mutter, and L. Wu, Contribution of volcanism and tectonism to axial and flank morphology of the southern East Pacific Rise, 17°10'-17°40', from a study of layer 2A geometry, *J. Geophys. Res.*, **102**, 10,165-10,184, 1997.
- Carbotte, S., C. Mutter, J. Mutter, and G. Ponce-Correa, Influence of magma supply and spreading rate on crustal magma bodies and emplacement of the extrusive layer: Insights from the East Pacific Rise at 16°N, *Geology*, **26**, 455-458, 1998.
- Christeson, G. L., G. M. Purdy, and G. J. Fryer, Structure of young upper crust at the East Pacific Rise near 9°30'N, *Geophys. Res. Lett.*, **19**, 1045-1048, 1992.
- Christeson, G. L., G. M. Purdy, and G. J. Fryer, Seismic constraints on shallow crustal emplacement processes at the fast spreading East Pacific Rise, *J. Geophys. Res.*, **99**, 17,957-17,974, 1994.
- Christeson, G. L., G. M. Kent, G. M. Purdy, and R. S. Detrick, Extrusive thickness variability at the East Pacific Rise, 9°-10°N: Constraints from seismic techniques, *J. Geophys. Res.*, **101**, 2859-2873, 1996.
- Cormier, M.-H., K. C. Macdonald, and D. S. Wilson, A three-dimensional analysis of the East Pacific Rise from 18° to 21°30'S, *J. Geophys. Res.*, **100**, 8063-8082, 1995.
- DeMets, C., R. G. Gordan, D. F. Argus, and S. Stein, Effect of recent revisions to the geomagnetic reversal time scale on estimates of current plate motions, *Geophys. Res. Lett.*, **21**, 2191-2194, 1994.
- Detrick, R. S., P. Buhl, E. Vera, J. C. Mutter, J. A. Orcutt, J. Madsen, and T. Brocher, Multi-channel seismic images of a crustal magma chamber along the East Pacific Rise, *Nature*, **326**, 35-41, 1987.
- Detrick, R. S., A. J. Harding, G. M. Kent, J. A. Orcutt, J. C. Mutter, and P. Buhl, Seismic structure of the southern East Pacific Rise, *Science*, **259**, 499-503, 1993.
- Fornari, D. J., R. M. Haymon, M. R. Perfit, T. K. P. Gregg, and M. H. Edwards, Axial summit trough of the East Pacific Rise 9°-10°N: Geological characteristics and evolution of the axial zone on fast spreading mid-ocean ridges, *J. Geophys. Res.*, **103**, 9827-9855, 1998.
- Francheteau, J., and R. D. Ballard, The East Pacific Rise near 21°N, 13°N and 20°S: Inferences for along-strike variability of axial processes of the mid-ocean ridge, *Earth Planet. Sci. Lett.*, **64**, 93-116, 1983.
- Gripp, A. E., and R. G. Gordan, Current plate velocities relative to the hotspots incorporating the NUVEL-1 global plate motion model, *Geophys. Res. Lett.*, **17**, 1109-1112, 1990.
- Harding, A. J., G. M. Kent and J. A. Orcutt, A multichannel seismic investigation of upper crustal structure at 9°N on the East Pacific Rise: Implications for crustal accretion, *J. Geophys. Res.*, **98**, 13,925-13,944, 1993.
- Haymon, R. M., D. J. Fornari, M. H. Edwards, S. Carbotte, D. Wright, and K. C. Macdonald, Hydrothermal vent distribution along the East Pacific Rise crest (9°09'-9°54' N) and its relationship to magmatic and tectonic processes on fast spreading ridges, *Earth Planet. Sci. Lett.*, **104**, 513-534, 1991.
- Hooft, E. E., H. Schouten, and R. S. Detrick, Constraining crustal emplacement processes from the variation in seismic Layer 2A thickness at the East Pacific Rise, *Earth Planet. Sci. Lett.*, **142**, 289-310, 1996.
- Hooft, E. E., R. S. Detrick, and G. M. Kent, Seismic structure and indicators of magma budget along the southern East Pacific Rise, *J. Geophys. Res.*, **102**, 27,319-27,340, 1997.
- Hussenoeder, S. A., J. A. Collins, G. M. Kent, R. S. Detrick, and the TERA Group, Seismic analysis of the axial magma chamber reflector along the southern East Pacific Rise from conventional reflection profiling, *J. Geophys. Res.*, **101**, 22,087-22,105, 1996.
- Kent, G. M., A. J. Harding, and J. A. Orcutt, Distribution of magma beneath the East Pacific Rise near the 9°03'N overlapping spreading center from forward modelling of common depth point data, *J. Geophys. Res.*, **98**, 13,971-13,995, 1993a.
- Kent, G. M., A. J. Harding, and J. A. Orcutt, Distribution of magma beneath the East Pacific Rise between the Clipperton transform and the 9°17'N Deval from forward modelling of common depth point data, *J. Geophys. Res.*, **98**, 13,945-13,696, 1993b.
- Kent, G. M., A. J. Harding, J. A. Orcutt, R. S. Detrick, J. C. Mutter, and P. Buhl, Uniform accretion of oceanic crust south of the Garrett transform at 14°15'S on the East Pacific Rise, *J. Geophys. Res.*, **99**, 9097-9116, 1994.
- Kent, G. M., R. S. Detrick, S. A. Swift, J. A. Collins, and I. I. Kim, Evidence from Hole 504B for the origin of dipping events in oceanic crustal reflection profiles as out-of-plane scattering from basement topography, *Geology*, **25**, 131-134, 1997.
- Klitgord, K. D., and J. D. Mudie, The Galapagos spreading center: A near bottom geophysical survey, *Geophys. J. R. Astron. Soc.*, **38**, 536-586, 1974.

- Langmuir, C. H., J. F. Bender, and R. Batiza, Petrologic and tectonic segmentation of the East Pacific Rise, 5°30'N-14°30'N, *Nature*, 322, 422-429, 1986.
- Langmuir, C., J. Bender, K. Donnelly, S. Shirey, M. Cormier, E. Baker, and PANRI Team, Petrology of the East Pacific Rise north of the Orozco transform fault, *EOS Trans. AGU*, Fall Meet. Suppl., 79 (45), F832, 1998.
- Lonsdale, P., The rise flank trails left by migrating offsets of the equatorial East Pacific Rise axis, *J. Geophys. Res.*, 94, 713-743, 1989.
- Macdonald, K. C., and P. J. Fox, The axial summit graben and cross-sectional shape of the East Pacific Rise as indicators of axial magma chambers and recent eruptions, *Earth Planet. Sci. Lett.*, 88, 119-131, 1988.
- Macdonald, K. C., J. -C. Sempere, and P. J. Fox, East Pacific Rise from Siqueiros to Orozco Fracture Zones: Along-strike continuity of axial neovolcanic zone and structure and evolution of overlapping spreading centers, *J. Geophys. Res.*, 89, 6049-6069, 1984.
- Macdonald, K. C., P. J. Fox, L. J. Perram, M. F. Eisen, R. M. Haymon, S. P. Miller, S. M. Carbotte, M.-H. Cormier, and A. N. Shor, A new view of the mid-ocean ridge from the behavior of ridge-axis discontinuities, *Nature*, 335, 217-225, 1988.
- Macdonald, K.C., et al., The East Pacific Rise and its flanks 8-18°N: History of segmentation, propagation, and spreading direction based on SeaMARC II and Sea Beam studies, *Mar. Geophys. Res.*, 14, 299-344, 1992.
- McClain, J. S., J. A. Orcutt, and M. Burnett, The East Pacific Rise in cross section: A seismic model, *J. Geophys. Res.*, 90, 8627-8639, 1985.
- Mutter, J. C., S. M. Carbotte, W. Su, L. Xu, P. Buhl, R. S. Detrick, G. M. Kent, J. A. Orcutt, and A. J. Harding, Seismic images of active magma systems beneath the East Pacific Rise between 17°05' and 17°35'S, *Science*, 268, 391-395, 1995.
- Phipps Morgan, J., and Y. J. Chen, The genesis of oceanic crust: Magma injection, hydrothermal circulation, and crustal flow, *J. Geophys. Res.*, 98, 6283-6297, 1993a.
- Phipps Morgan, J., and Y. J. Chen, Dependence of ridge-axis morphology on magma supply and spreading rate, *Nature*, 364, 706-708, 1993b.
- Ponce-Correa, G., J. Mutter, S. Carbotte, Fresnel zone: A pitfall in seismic imaging of mid-ocean ridge magma lenses, *Geophys. Res. Lett.*, 29, 3021-3024, 1999.
- Scheirer, D. S., and K. C. Macdonald, Variation in cross-sectional area of the axial ridge along the East Pacific Rise: Evidence for the magmatic budget of a fast spreading center, *J. Geophys. Res.*, 98, 7871-7885, 1993.
- Sempere, J. C., J. R. Cochran, and the SEIR Team, The Southeast Indian Ridge between 88°E and 118°E: Variations in crustal accretion at constant spreading rate, *J. Geophys. Res.*, 102, 15,489-15,505, 1997.
- Sloan, H., Temporal evolution of overlapping spreading centers at 16°20'N on the East Pacific Rise, *Mar. Geol.*, 97, 315-324, 1991.
- Slotnick, M. M., *Lessons in Seismic Computing*, 268 pp., Soc. of Explor. Geophys., Tulsa, Okla., 1959.
- Small, C., A global analysis of mid-ocean ridge axial topography, *Geophys. J. Int.* 116, 64-84, 1994.
- Small, C., and D. T. Sandwell, An analysis of ridge axis gravity roughness and spreading rate, *J. Geophys. Res.*, 97, 3235-3245, 1992.
- Smith, W. H. F., and P. Wessel, Gridding with continuous curvature splines in tension, *Geophysics*, 55, 293-305, 1990.
- Tolstoy, M., A. J. Harding, and J. A. Orcutt, Deepening of the axial magma chamber on the East Pacific Rise toward the Garrett Fracture Zone, *J. Geophys. Res.*, 102, 3097-3108, 1997.
- Toomey, D. R., G. M. Purdy, S. C. Solomon, and W. S. D. Wilcock, The three-dimensional seismic velocity structure of the East Pacific Rise near latitude 9°30'N, *Nature*, 347, 639-645, 1990.
- Toomey, D. R., S. C. Solomon, and G. M. Purdy, Tomographic imaging of the shallow crustal structure of the East Pacific Rise at 9°30'N, *J. Geophys. Res.*, 99, 24,135-24,157, 1994.
- Vera, E. E., and J. B. Diebold, Seismic imaging of oceanic layer 2A between 9°30'N and 10°N on the East Pacific Rise from two-ship wide-aperture profiles, *J. Geophys. Res.*, 99, 3031-3041, 1994.
- Vera, E. E., P. Buhl, J. C. Mutter, A. J. Harding, J. A. Orcutt, and R. S. Detrick, The structure of 0-0.2 My old oceanic crust at 9°N in the East Pacific Rise from expanded spread profiles, *J. Geophys. Res.*, 95, 15,529-15,556, 1990.
- Wang, X., and J. R. Cochran, Along-axis gravity gradients at mid-ocean ridges: Implications for mantle flow and axial topography, *Geology*, 23, 29-32, 1995.
- Wang, X., J.R. Cochran, and G.A. Barth, Gravity anomalies, crustal thickness and the pattern of mantle flow at the fast spreading East Pacific Rise, 9°-10°N: Evidence for three-dimensional upwelling, *J. Geophys. Res.*, 101, 17,927-17,940, 1996.
- Weiland, C. M., and K. C. Macdonald, Geophysical study of the East Pacific Rise 15°-17°N: An unusually robust segment, *J. Geophys. Res.*, 101, 20,257-20,274, 1996.
- Whitehead, J.A., H.J.B. Dick, and H. Schouten, A mechanism for magma accretion under spreading centers, *Nature*, 312, 146-147, 1984.
- Wilcock, W. S. D., S. C. Solomon, G. M. Purdy, and D. R. Toomey, The seismic attenuation structure of a fast-spreading mid-ocean ridge, *Science*, 258, 1470-1474, 1992.

S.M. Carbotte, and G. Ponce-Correa, Lamont-Doherty Earth Observatory of Columbia University, Box 1000, Palisades, NY 10964. (carbotte@ldeo.columbia.edu)

A. Solomon, Bryn Mawr College, 101 N. Merion Ave., Bryn Mawr, PA 19010.

(Received October 16, 1998; revised May 26, 1999; accepted July 12, 1999.)